Simulation of Flow around a Circular Pier on a Scoured Bed using CFD Modelling Software

A thesis submitted towards partial fulfilment of the requirements for the degree of

Master of Engineering

in

Water Resources and Hydraulic Engineering

Submitted by

ANIMESH DAS

Exam. Roll No. - M6WRP24006

Registration No. – 160493 of 2021-2022

Under the guidance of

Dr. SUBHASISH DAS

Associate Professor

School of Water Resources Engineering, Jadavpur University

&

Dr. GOURAB BANERJEE

Assistant Professor

School of Water Resources Engineering, Jadavpur University

School of Water Resources Engineering

M.E. (Water Resources & Hydraulic Engineering)

Course affiliated to ***Faculty Council of Engineering & Technology***

Jadavpur University

Kolkata-700032, West Bengal, India

2024

Declaration of Originality and Compliance of Academic Ethics

I hereby declare that this thesis contains a literature survey and original research work by the undersigned candidate, as part of my **Master of Engineering** in **Water Resources and Hydraulic Engineering** in the Faculty Council of Interdisciplinary Studies, Law & Management, Jadavpur University during the academic session 2023-24.

All information in this document have been obtained and presented in accordance with academic rules and ethical conduct.

I also declare that, as required by these rules and conduct, I have fully cited and referenced all material and results that are not original to this work.

Name : **Animesh Das**

Exam. Roll Number : **M6WRP24006**

Thesis Title : **Simulation of Flow around a Circular Pier on a Scoured Bed using CFD Modelling Software**

Signature with Date :

M.E. (Water Resources & Hydraulic Engg.) course affiliated to
Faculty Council of Engineering & Technology
Jadavpur University
Kolkata, India

Certificate of Recommendation

This is to certify that the thesis entitled **"*Simulation of Flow around a Circular Pier on a Scoured Bed using CFD Modelling Software*"** is a bonafide work carried out by **Mr. Animesh Das** under my supervision and guidance for partial fulfillment of the requirement for the Post Graduate Degree of Master of Engineering in Water Resources and Hydraulic Engineering during the academic session 2023-24.

THESIS ADVISOR
Dr. Subhasish Das
Associate Professor
School of Water Resources Engineering
Jadavpur University

THESIS ADVISOR
Dr. Gourab Banerjee
Assistant Professor
School of Water Resources Engineering
Jadavpur University

DIRECTOR
Prof. (Dr.) Asis Mazumdar
School of Water Resources Engineering
Jadavpur University

DEAN
Prof. (Dr.) Ratan Mondal
Faculty Council of Interdisciplinary Studies, Law & Management
Jadavpur University

M.E. (Water Resources & Hydraulic Engg.) course affiliated to
Faculty Council of Engineering &Technology
Jadavpur University
Kolkata, India

CERTIFICATE OF APPROVAL**

This foregoing thesis is hereby approved as a credible study of an engineering subject carried out and presented in a manner satisfactory to warrant its acceptance as a prerequisite to the degree for which it has been submitted. It is understood that by this approval the undersigned do not endorse or approve any statement made or opinion expressed or conclusion drawn therein but approve the thesis only for the purpose for which it has been submitted.

_____

Committee of
Final
Examination for
the evaluation
of the thesis

_____

_____

**Only in case the thesis is approved.

ACKNOWLEDGEMENTS

I express my sincere gratitude to my supervisors, ***Dr. Subhasish Das,*** *Associate Professor and* ***Dr. Gourab Banerjee****, Assistant Professor of School of Water Resources Engineering, Jadavpur University, under whose supervision and guidance this work has been carried out. It would have been impossible to carry out this thesis work with confidence without their wholehearted involvement, advice, support and constant encouragement throughout. They have not only helped me in carrying out my thesis but also have given me valuable advice to proceed further in my life.*

I would also express my sincere gratitude to ***Prof. (Dr.) Asis Mazumdar, Prof. (Dr). Pankaj Kumar Roy,*** *and* ***Dr. Rajib Das*** *Faculty members of School of Water Resources Engineering, Jadavpur University for their valuable suggestions.*

Special thanks to ***Mr. Plabon Sen*** *for his invaluable assistance in helping me learn ANSYS and successfully run simulations.*

I also express my sincere thanks to ***Mr. Saikat Mondal and Mr. Buddhadev Nandi*** *Research Scholars of the School of Water Resources Engineering, Jadavpur University for their unconditional support and affection during my work. Also, thanks to my classmates* ***Mr. Sourav Samaddar, Mr. Sudarshan Mondal*** *and* ***Ms. Nibedita Roy*** *for their help.*

Thanks are also due to all staff of the School of Water Resources Engineering and the Regional-cum-Facilitation Centre (RCFC), NMPB, Jadavpur University for their help and support.

Date :

Place : Jadavpur University

Mr. Animesh Das
Exam. Roll No: M6WRP24006

Abstract

Bridges are an important part of a transportation network. Piers on which the superstructure of the bridge is provided are important components for the stability and safety of the bridge. There are many cases of failure of bridges due to scouring at their foundations. The scour around the piers is caused due to changes in flow patterns around piers due to the three-dimensional separation of the boundary layer, which has a large magnitude of turbulence and vortices around the piers. For designing pier foundations, it is very essential to estimate the correct depth of scour below river bed level since it affects the depth of the foundation and ultimately the cost of the bridge. The present study is directly relevant to understanding erosion mechanisms around a circular bridge pier model constructed in a river bend.

In this research, a Unsteady Reynolds Averaged Navier–Stokes (URANS) approach is applied, to enable the simulation of scouring around the bridge pier model. This methodology allows an approach that numerically describes a complex three-dimensional (3D) scour behavior around bridge piers by coupling the changes in topography with the local detailed hydrodynamics. By using a commercial Computational Fluid Dynamics (CFD) tool, ANSYS in order to calculate scour. The dynamic mesh updating technique is implemented to move the bed and assures a practical and accurate scour simulation by individually updating the domain's riverbed at each time step. Simulation, in accordance with the experimental configuration of Dargahi (1989) for the turbulent channel flow past a circular cylinder, mounted in a flatbed, has been undertaken using the RANS approach. The projected results have been compared with those obtained from URANS models (i.e., k-ε standard and k-ω SST (Shear Stress Transport), and with the experimental data, in order to verify the reliability and feasibility of the URANS.

The coupling between RANS and the dynamic mesh technique has been undertaken to study the coherent structures around a circular bridge pier model in the initial stage of scour evolution. The approach produces a good prediction of the qualitative and quantitative characteristics observed by the experiment of Dargahi (1989). Furthermore, studying the transient behavior of the horseshoe vortex system upstream of the circular pier model, during the scour process evolution shows that the main vortex has the bimodal oscillation phenomenon, which increases the ability of these vortices to remove the sediment around the circular pier model.

Content

Chapter No	Topics	Page No
	Declaration	iii
	Certificate of Recommendation	v
	Certificate of Approval	vii
	Acknowledgements	ix
	Abstract	xi
Chapter 1		
	1.1 Introduction	1
	1.2 Scour	3
	1.2.1 Classification of scour	4
	1.2.2 Local scour	4
	1.3 Local scour mechanism	6
	1.4 Horseshoe vortex	7
	1.5 Wake vortex	8
	1.6 Parameters Influencing Scour	9
	1.6.1 Flow intensity	9
	1.6.2 Flow depth	9
	1.6.3 Pier width	10
	1.6.4 Pier Shape	10
	1.6.5 Sediment Size	11
	1.6.6 Flow Froude Number	11
	1.6.7 Angle of repose	11
	1.7 CFD Modelling	12
	1.7.1 Mathematical Formulation	12
	1.7.2 Discretization	13
	1.7.3 Mesh Generation	13
	1.7.4 Boundary Conditions	13
	1.7.5 Solver Selection	13
	1.7.6 Solution Process	13
	1.7.7 Turbulence Modeling	13
	1.7.8 Post-Processing and Visualization	14
	1.7.9 Validation and Verification	14
	1.7.10 Applications and Benefits	14
	1.7.11 Challenges and Considerations	14
	1.8 Ansys Fluent	14
	1.9 Governing equations	15
	1.10 Unsteady Reynolds-Averaged Navier-Stokes (URANS)	15
	1.11 Eulerian multiphase model and k- ε turbulence model	16
	1.11.1 Transport Equations for the Standard k- ε Model	17
	1.12 Modeling the Turbulent Viscosity	18
	1.13 Model Constants	18
	1.14 Vortex shedding and Strouhal number	18
	1.15 Pressure coefficient	18
	1.16 Dynamics of horseshoe vortex and scour mechanisms	19
	1.17 Sediment transport modelling	19
	1.17.1 Incipient motion of sediment	20
	1.17.2 Rate of sediment transport	20

Chapter 2	**Literature Review**	22
Chapter 3	**Objectives and Methodology**	
	3.1 Objectives	27
	3.2 Configuration investigated	27
	3.3 Named Selections	28
	3.4 Solution method	29
	3.5 Boundary conditions	30
Chapter 4	**Results and Discussion**	
	4.1 Flow past a Circular Pier Model mounted on a Flat Bed	31
	4.1.1 Mean flow and turbulence statistics	31
	4.2 Vortex shedding and Strouhal number	34
	4.3 Mean pressure distributions	37
	4.4 Bed shear stress	40
	4.5 Three-dimensional dynamics of the horseshoe vortex and scour mechanisms	41
Chapter 5	**Summary and Findings**	44
Chapter 6	**Conclusions and Further work**	46
	6.1Conclusions	46
	6.2Further work	46
	6.3 References	47

List of Figures:

Sl No.	Fig	Page No.
1	**Fig 1.1** Reason behind Scour	04
2	**Fig 1.2** Types of Scour	04
3	**Fig 1.3** Flow disturbance around a cylindrical pier (Arneson et al. 2012).	07
4	**Fig 1.4** Mechanism of horseshoe vortex	08
5	**Fig 3.1** Experimental setup for numerical simulation	28
6	**Fig 3.2** Meshing for numerical simulation	28
	Fig 3.3 Named Selections of Geometry	29
7	**Fig 4.1** Mesh independency study for *k*-ε standard model (Fig a, b and c), and *k*-ω SST model (Fig d, e and f).	32
8	**Fig 4.2** Horseshoe vortices upstream of the circular pier model	33
9	**Fig 4.3** Instantaneous horseshoe vortex system at the symmetry plane in front of the circular pier model (a) reported by Dargahi (1989), (b) *k*-ε standard model and (c) *k*-ω SST model.	34
10	**Fig 4.4** Velocity magnitude streamlines using *k*-ε standard.	36
11	**Fig 4.5** Velocity magnitude streamlines downstream of the circular pier model at every 0.5 second using *k*-ω SST	37
12	**Fig 4.6** velocity magnitude behind the circular pier model at a difference of 0.5 seconds.	37
13	**Fig 4.7** Pressure coefficient along the line of symmetry upstream of a circular pier model	38
14	**Fig 4.8** Pressure coefficient along the stagnation line at the upstream of a circular pier model.	39
15	**Fig 4.9** Pressure coefficient at the free surface and along the line of symmetry.	40

16	**Fig 4.10** Mean bed shear stresses along the line of symmetry upstream of a circular pier model.	41
17	**Fig 4.11** Visualization of the instantaneous 3D coherent structures around the circular pier model using URANS models.	42
18	**Fig 4.12** The maximum scour for the first 100 seconds of scour initiation using k-ε standard and k-ω SST.	43

List of Tables:

Sl No.	Tables	Page No.
1	**Table 3.1** Dimensions of the flow studied, with the corresponding Reynolds and Froude numbers.	27
	Table 3.2 CFD setup parameters	29
2	**Table 3.3** Boundary Conditions	30
3	**Table 4.1** Summary of predicted drag coefficient, C_d, and downstream vortex shedding parameters for circular circular pier model using FFT method and visualization method.	35

Nomenclature

The following symbols are used in this dissertation work:

2-D	=	Two-dimensional;
3-D	=	Two-dimensional;
CFL	=	Courant-Friedrichs-Lewy Number;
CFD	=	Computational Fluid Dynamics;
FFT	=	Fast Fourier Transform;
PSD	=	Power Spectral Density;
DES	=	Detached Eddy Simulation;
RANS	=	Reynolds Averaged Navier- Stokes model;
SGS	=	Subgrid-Scale model;
LES	=	Large Eddy Simulation model;
RSM	=	Reynolds Stress Equation Model;
URANS	=	Unsteady Reynolds-Averaged Navier Stokes model;
UDF	=	User Defined Function
D	=	Diameter of the Circular pier model [L];
d_{50}	=	Median diameter of sand [L];
F_r	=	Froude number of flow [—];
g	=	Gravitational acceleration [LT^{-2}];
H	=	Approaching flow depth [L];
l_s	=	Scour length [L];
Q	=	Second invariant of the velocity gradient tensor [T^{-2}];
R_e	=	Flow Reynolds number [—];
R_p	=	Pier Reynolds number [—];
U_∞	=	Depth-averaged approaching flow velocity [LT^{-1}];
u_i	=	Represents velocity component in corresponding direction [LT^{-1}];
$u_{i'}$	=	Velocity fluctuations due to turbulence in corresponding direction [LT^{-1}];
u_*	=	Shear velocity [LT^{-1}];
u_{*c}	=	Critical shear velocity [LT^{-1}];
ρ	=	Mass density of fluid [ML^{-3}];
ρ_s	=	Mass density of sand [ML^{-3}];
υ	=	Kinematic viscosity [L^2T^{-1}];
μ	=	Dynamic viscosity [$ML^{-1}T^{-1}$];
μ_t	=	Turbulent or eddy viscosity [$ML^{-1}T^{-1}$];
μ_t	=	Turbulent or eddy viscosity [$ML^{-1}T^{-1}$];
M_t	=	Turbulent Mach number [—];
a	=	Speed of sound [LT^{-1}];
γ	=	Adiabatic constant [—];
R	=	Molar gas constant [$M^{1} L^{2} T^{-2} K^{-1}$];
T	=	Absolute Temperature [K];
β	=	Co-efficient of thermal expansion [K-1];
k	=	Turbulence kinetic energy [L^2T^{-2}];
ε	=	Turbulent kinetic energy dissipation rate [L^2T^{-3}];
σ_k	=	Turbulent Prandtl number for k [—];

G_k	=	Production of turbulent kinetic energy (TKE) due to mean velocity shear [L^2T^{-2}];
G_b	=	Production of turbulent kinetic energy (TKE) due to buoyancy [L^2T^{-2}];
Δ_t	=	Time-step size [T];
θ_{cr}	=	Critical shield number [—];
s	=	Relative density of sediment [ML^{-3}];
n	=	Sediment void ratio [—];
h	=	River bed elevation [L];
τ_b	=	Sediment shear stress [$M^1L^{-1}T^{-2}$];
$\tau_{b.cr}$	=	Critical sediment shear stress [$M^1L^{-1}T^{-2}$];
τ_{ij}	=	Sub-grid-scale stress [$M^1L^{-1}T^{-2}$];
τ_{kk}	=	Isotropic part of the Sub-grid-scale stress [$M^1L^{-1}T^{-2}$];
S_{ij}	=	Rate of Strain tensor [T^{-1}];
K	=	von-Karman Constant [L];
L_s	=	Mixing length for Sub-grid scale [L];
d	=	Distance to the closest wall [L];
S_t	=	Strouhal number [—];
f_s	=	Shedding frequency [T^{-1}];
T_1	=	Period of one complete vortex shedding [T^{-1}];
C_p	=	Pressure coefficient [$M^1L^{-1}T^{-2}$];
Ω	=	Absolute value of vorticity [T^{-1}];
ω_{ij}	=	Angular velocity tensor [T^{-1}];
T	=	Dimensionless critical shear stress [—];

Glossary of terms

Bed load

Sediment grains roll, or are dragged, across the stream bed surface but are not lifted into suspension.

Clear-water transport

There is no sediment transport already coming from upstream.

Live-bed transport

There is already incoming sediment transport which originated further upstream.

Multiphase flow

Two or more fluids are flowing within the same volumetric space.

Packing limit

The maximum volume of a granular phase material which can be packed into a volume space, expressed as a proportion. (Takes account of void space).

Suspended load

Sediment grains are lifted into suspension and carried by the fluid flow.

Volume fraction

The proportion of a volume space is occupied by a particular secondary phase material.

FFT

The Fast Fourier Transform (FFT) is an efficient algorithm for computing the Discrete Fourier Transform (DFT) of a sequence of data points. It's particularly useful for analyzing and transforming data in the frequency domain, revealing the frequency components present in a signal or dataset.

URANS

The Unsteady Reynolds-Averaged Navier-Stokes (URANS) model is a computational fluid dynamics (CFD) approach used to simulate fluid flow. It combines the Reynolds-Averaged Navier-Stokes (RANS) equations with time-dependent terms to capture unsteady or transient flow phenomena. RANS equations average the Navier-Stokes equations over time to simplify the simulation of turbulent flows by separating the flow into mean and fluctuating components.

Chapter 1

1.1 Introduction

In civil engineering and construction, scouring refers to the removal of material (such as soil or sediment) from around structures (such as bridge foundations or culverts) due to the erosive force of water flow. Scouring around structures can compromise their stability and structural integrity, making it an important consideration in infrastructure design and maintenance. Overall, scouring involves the removal of material, whether it be sediment, impurities from fibers, or soil around structures, typically due to the action of water or other external forces.

This phenomenon happens in both flowing water and coastal areas. It is brought on by waves and water erosion removing silt from the area surrounding structures. Floods are often blamed for bridge failures because they remove bed material from the area surrounding the bridge foundations. The term "scour" describes the erosion of the earth around a bridge foundation, including the piers and abutments. This erosion can be brought on by water moving across the riverbed and dislodging materials from the bridge construction. In extreme circumstances, this erosion can erode the bridge foundation and cause scour holes, which can lead to bridge collapses. Building bridges in alluvial channels causes the waterway near the bridge site leading to increased water velocity, which exacerbates the scour phenomena.

Local, contraction, and degradation scour are the three main types of scours that typically have an impact on the functionality and safety of bridges. Water moving through piers or abutments has the potential to scour holes by removing silt from the area surrounding the pier. Horse vortex and down flow creation in front of the piers are the main causes of this sediment removal.

Wake vortices are created when the flow, which has been separated by the pier, converges downstream of the pier. The strength of the horseshoe vortex decreases with an increase in scour depth, thus leading to a decrease in the sediment transport rate from the pier base. Accurately predicting the formation of local scour is a crucial factor in bridge foundation design. Although forecasting bridge scour events has gained the attention of many researchers, it has proven difficult to predict scour behavior with a high degree of accuracy thus far.

A number of bridge failures that happened after 2000 have been documented here based on information from different literatures. On March 4, 2001, the Hintze Ribeiro Bridge, a reinforced cement concrete structure located in Castelo de Paiva, northern Portugal, collapsed as a result of piers' scouring, as depicted in. The accident claimed the lives of fifty-nine people, and the crumbling section also crushed three cars. The bridge was demolished and rebuilt after the accident, and hundreds of other bridges in the Portugal region were closed for urgent maintenance. The second-longest bridge in the world, the Queen Isabella Causeway in Texas, collapsed on September 15, 2001 as a result of pier failure. The collapse had a major economic impact on the area since the Causeway is the

only means to get from South Padre Island to Port Isabel. The Valigonda train disaster occurred in Valigonda, Hyderabad, India, on October 29, 2005. The June 2006 floods in northern Pennsylvania and upstate New York caused Interstate 88 to wash out. Bijapur Bridge collapse - In August 2007, a bridge over the Krishna River in Bijapur, Karnataka, collapsed due to scouring. The bridge was built in 1972, and the incident resulted in the loss of several lives. Kosi Bridge collapse - In August 2008, a bridge over the Kosi River in Bihar collapsed due to heavy floods and scouring. The bridge was a part of the National Highway-57 and was a vital link between Bihar and Nepal. Because of tidal scouring of the foundations, a 20-meter section of the Broadmeadow viaduct railway bridge in Ireland collapsed in August 2009. In November 2009, seven bridges in England were demolished or irreparably damaged as a result of heavy rains and flooding. According to the Colorado Department of Transportation's projections, in 2013 at least thirty state highway bridges were destroyed and twenty experienced significant flood damage (Novey). Scouring from water caused CPR Bonnybrook Ridge in Calgary, Canada, to partially collapse in 2013. One of the most notable instances of popular Greek architecture, the Plaka Bridge over the Arachthos River in Greece, collapsed on February 1, 2015 due to a flash flood. In August 2016, a bridge over the Savitri River in Mahad, Maharashtra, collapsed due to heavy floods and scouring. The bridge was built in 1928 and was a vital link between Mumbai and Goa. The incident resulted in the loss of several lives, and the bridge had to be rebuilt. Last but not least, on July 25, 2022, a bridge across the Kaliasot River in Madhya Pradesh, India, collapsed early this morning as a result of the year's intense rains. It has been stated that there is a very high likelihood of bridge failure as a result. The aforementioned investigation indicates that one of the main problems with bridge safety worldwide is bridge scour.

In the United States, approximately 60% of bridge failures are related to scour-based hydraulic deficiencies (Richardson 1999; Deng and Cai 2010). In 1987, a catastrophic collapse of the Schoharie Creek Bridge in New York was caused by the cumulative effects of bridge scour and a severe flood (NTSB 1988; Lagasse and Richardson 2001). The Los Gatos Creek Bridge over I-5 in the state of California collapsed due to the impact of flowing water during a flood event, and the underlying reason was attributed to local pier scouring from 28 years of service (Lagasse and Richardson 2001).

One of the main reasons for bridge failure is scour around the bridge pier. Due to sediment movement and three-dimensional flow, scour is an extremely complex phenomenon. Numerous scholars have used both theoretical analysis and experimentation to investigate the flow characteristics surrounding bridge piers. Scour is one of the primary causes of bridge failure, according to (Smith 1976) review of the causes of bridge failures worldwide from 1847 to 1975. According to (Huber 1991), since 1950, about 500 bridges have broken in the United States, with the majority of these failures being caused by scour of the foundation material. There is very little information about scour-related bridge failure in India. However, it is known that the nation's railroad bridges underwent hydrological and scour studies thanks to the efforts of the Research, Designs and Standards Organization (RDSO) in Lucknow.

Numerous research on scour near uniform piers and several methods to lessen scour are documented in the literature. However, there aren't many studies that have been done and published about the flow field surrounding bridge components. The majority of the

laboratory research conducted by the investigators (Melville and Raudkivi, 1977; Ahmed and Rajaratnam, 1998; Graf and Istiarto, 2002; Dey and Raikar, 2007) has been done inside scour holes surrounding uniform circular piers.

Many previous studies have focused on the methodologies and techniques to analyze local bridge scour using experimental tests (Melville, 1975; Abed and Gasser, 1993; Umbrell et al., 1998; Ataie-Ashtiani and Beheshti, 2006; Deng and Cai, 2010; Xiong et al., 2012). However, such experimental scour tests are mostly conducted for large-scale and important bridges since they are expensive and labor-intensive. For most common highway bridges, nevertheless, experimental tests are not applicable even though scour more often occurs at such ordinary bridges. In addition, some researchers have investigated analytical solutions to the bridge scour due to their practical conveniences and economic advantages (Federal Highway Administration, 1993; Jain and Fischer, 1979; Melville and Sutherland, 1988; Froehlich, 1989); and important conclusions have been incorporated in the current design codes (Federal Highway Administration, 1993).

The main drawback of these analytical methods is they are mostly based on an assumption that the scour events are limited to one-dimensional conditions with only one parameter which is the scour depth. Actual bridge scour, on the contrary, often develops in a much more complicated three-dimensional (3D) behavior, which has several time-dependent parameters such as the scour depths, scour hole profiles, flow fields, etc. Thus, this dimensional discrepancy may result in substantial errors between simulations and realities.

The 3D scour simulation method has become more and more popular in recent decades (Kassem et al., 2003; Chiew, 2004; Ataie-Ashtiani and Beheshti, 2006; Benedict et al., 2007; Zhang et al., 2009; Kumar et al., 2012; Ramamurthy et al., 2013). For example, Kassem et al. (2003) developed a numerical model to simulate the field scour data, which was verified by the measurements obtained in the laboratory. Zhang et al. (2009) developed a 3D model to simulate the complex local flow field around the scour area using the finite-volume method. These simulations all assumed that the running water under a clear-water environment predominantly induces most of the interactions between the flow and the riverbed.

1.2 Scour

Scouring is a natural phenomenon generated by the passage of water in a river or stream. Although it is most obvious in alluvial materials, badly eroded rock can also be vulnerable in certain circumstances. It results from the erosive action of moving water, which disintegrates and erodes material from the stream bed and banks as well as the area of bridge piers and abutments. Scouring occurs naturally as a result of both man-made constructions and changes in river shape. The main reasons behind the scour are Depth of flow, Pier width, Velocity of flow, field Froude number and Bed materials. One of the primary reasons (Fig. 1.1) for bridge failure is scour. The scour destroys the bed materials around the bridge's foundation, exposing the foundation and jeopardizing the bridge's stability.

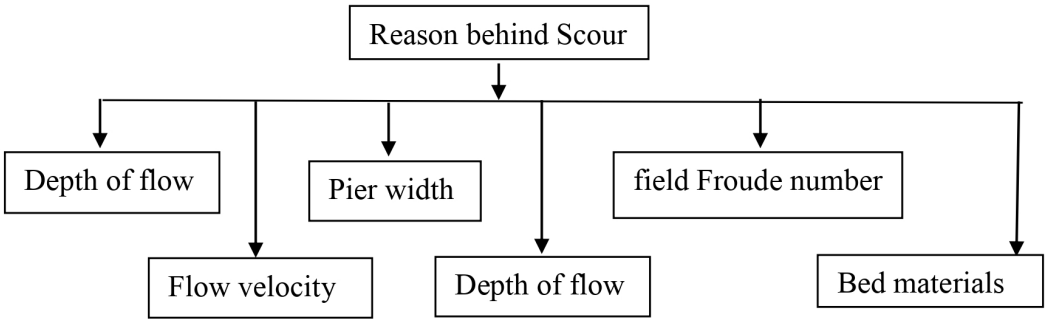


Fig 1.1 Reasons behind scour

1.2.1 Classification of scour

Regardless of whether a structure is present, general scour happens in a river or stream as a result of natural processes. Man-made buildings or any other hazard may also induce scour in the river bed. Scour is divided into two types: (a) widespread scour and (b) localized scour. In addition, further sub-divisions of scour are depicted in Fig 1.2.

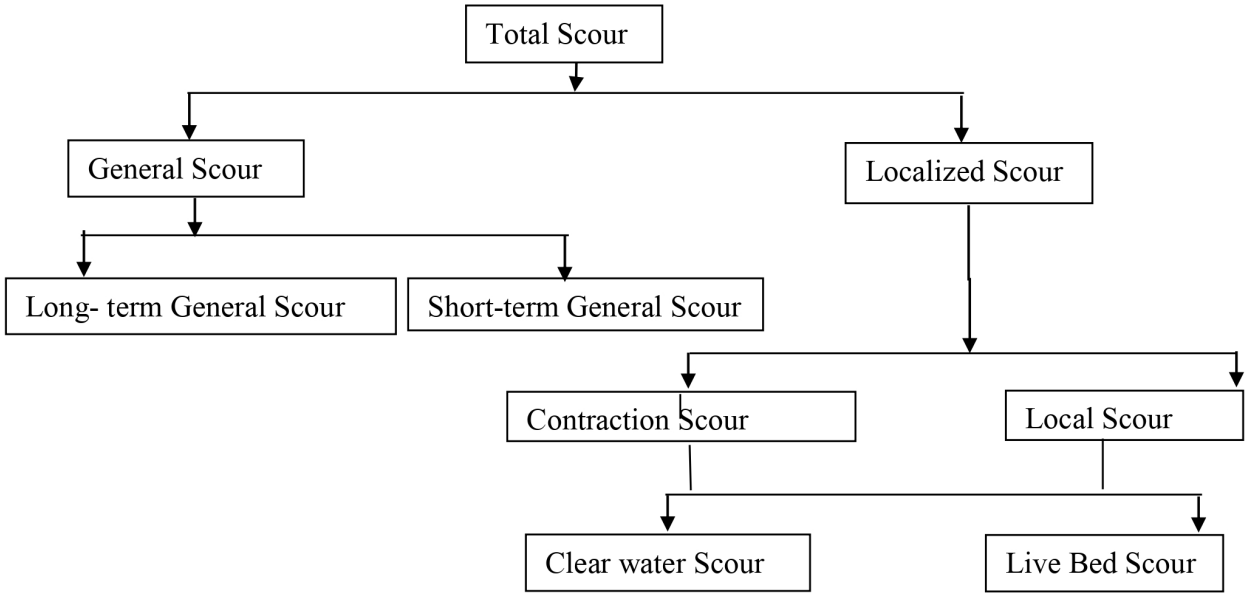


Fig 1.2 Types of scour

1.2.2 Local scour

Erosion that occurs close to a pier, an abutment, an erosion control mechanism, or a similar impediment to the flow is referred to as local scour. These obstructions accelerate the flow and cause vortices that remove the surrounding sediments. Most of the time, local scour depths are ten times greater than general or contraction scour depths. By reducing the

stability of riprap revetments and other structures, local scour can lead to collapses. The following elements affect regional scour:

- Width of the obstruction.
- Projection length of the obstruction into the flow.
- Length of the obstruction.
- Angle of the approach flow.
- Velocity of the approach flow.
- Size of the bed material.
- Depth of flow.
- Shape of the obstruction.
- Bed configuration.

The width of the obstacle has a direct impact on the depth of the scour. Therefore, the scour will be deeper the wider the blockage. The ratio of obstruction width to channel width is likely a more accurate indicator of scour potential than obstruction width alone, while not being covered by most empirical relations. The depth of the scour is influenced by the predicted length of the barrier in the stream. The amount of scour increases as an abutment's projected length into the flow lengthens.

The depth of the scour can increase with length, but only to a certain point. When the ratio of the projected length of the stream to the depth of the approaching flow is approximately 25, this limit is reached. For straight sections, a structure's stream-wise length has no discernible impact on the scour depth; however, when the structure is at an angle to the flow, the length has a significant impact. When a structure's length is doubled, the scour depth rises by as much as 33% at the same angle of attack. Some equations incorporate the length factor by using the ratio of the structure's length to the flow's depth or width as well as the flow's angle of attack on the structure. Others incorporate flow in their equations using the projected area of the structure.

With an increase in flow depth, the scour depth may grow by a factor of two or more. The increase for bridge abutments varies from 1.1 to 2.15 depending on the abutment's shape. The scour depth increases together with the velocity of the approach flow. The size of the bed material affects scour depth even though the effect is primarily a function of the amount of time exposed to erosive flows. To put it another way, the size of the sediment may only have an effect on how long it takes to reach the maximum or ultimate scour. Large bed component particles, such as boulders or cobbles, could protect the scour hole's plate.

Local scour is greatly influenced by the shape of the structure as well as the flow's angle of attack on an obstruction. Structures that are angled to cause flow convergence tend to increase scour, whereas structures that are angled to cause flow divergence tend to reduce scour. Streamlined structures effectively lower ultimate scour depths by weakening the horseshoe and wake vortices. The shape of the bed (bed configuration) in streams with sand beds influences the flow velocity and turbulence, which in turn influences the depth of the scour. Both the local and global (contraction) scour can be accelerated by ice and debris. The extent of the growth is still largely unknown.

1.3 Scour mechanism

A cylindrical pier causes a three-dimensional separation of the boundary layer flow. In front of the element, a vortex system created by this divided shear layer rolls up along the barrier and is carried downstream by the river flow. Viewed from the top, this vortex system has the characteristic shape of a horseshoe and is thus called a horseshoe vortex (Fig 1.3). A local enhancement in the flow's ability to move material is caused by the creation of the horseshoe vortex and the down flow that surrounds the cylindrical pier. This results in the formation of a large hole (scour hole) around the cylindrical pier, which alters the flow pattern and lowers the flow's ability to convey sediment by reducing shear stress. Therefore, the features of flow, pier, and river-bed material largely determine the temporal fluctuation of scour and the maximum depth of scour at bridge elements. The horseshoe vortex's development and the resulting down flow result in scour at the spur dike, abutment, and cylindrical pier.

The mechanism of local scour can be described in several stages. Initially, the flow approaching the structure is deflected as it encounters the obstruction, creating zones of high velocity and turbulence around the pier. This deflection causes the flow velocity immediately downstream of the pier to increase, forming a horseshoe-shaped vortex pattern. This vortex induces strong scouring action on the riverbed, leading to the erosion of sediment particles.

As the process continues, the scour hole begins to deepen and expand around the pier. The horseshoe vortex intensifies the erosive forces, eroding the bed material and transporting sediment away from the scour hole. The sediment is then carried downstream by the flow.

Over time, the shape and size of the scour hole may change due to variations in flow conditions and sediment characteristics. It can deepen vertically or widen horizontally, depending on factors such as flow velocity, sediment type, and pier geometry. The presence of obstructions or irregularities in the channel can also influence the local scour pattern.

The mechanism of scour around bridge piers was studied by Kothyari *et al.* (1992*a*, *b*) whereas studies on the mechanism of scour around abutments and spur dikes are available in Kothyari and Ranga Raju (2001).

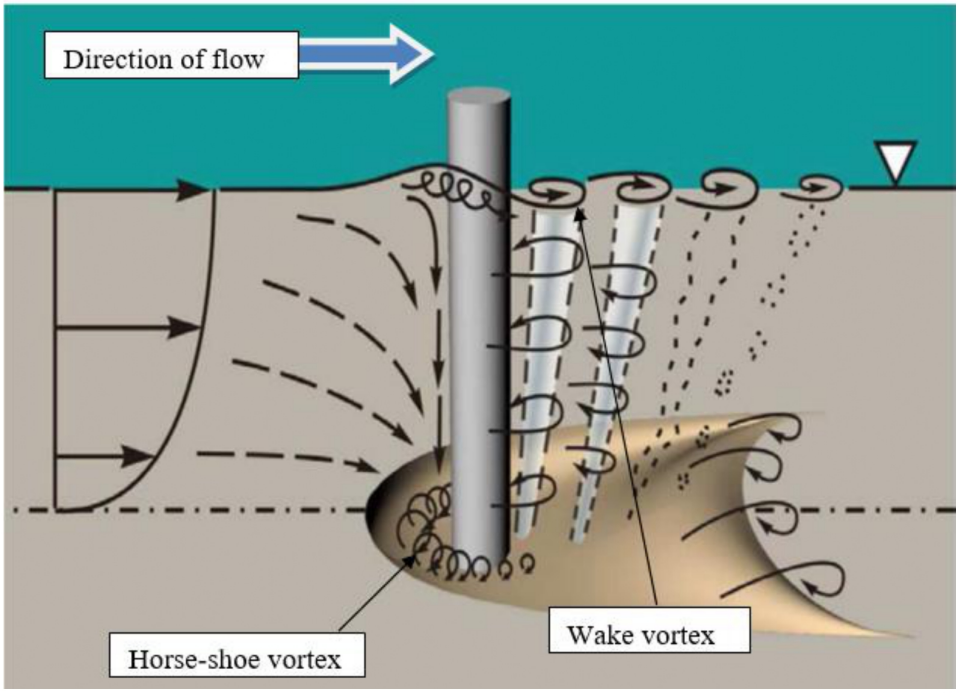


Fig 1.3 Flow disturbance around a cylindrical pier (Arneson et al., 2012).

1.4 Horseshoe vortex

The horseshoe vortex and down-flow are two significant hydrodynamic components that play a crucial role in local scour around bridge piers or other structures in rivers or channels. The horseshoe vortex is formed when flowing water encounters an obstruction, such as a bridge pier. As the water approaches the pier, it is deflected, creating a region of high velocity and turbulence. This results in the formation of a horseshoe-shaped vortex pattern around the pier. The flow near the pier is separated into two branches: an upward-flowing branch on the upstream side and a downward-flowing branch on the downstream side. This horseshoe vortex induces strong scouring action on the riverbed, contributing to the erosion and removal of sediment.

The downward-flowing branch of the horseshoe vortex commonly referred to as the down-flow, plays a significant role in local scour processes. The down-flow occurs on the downstream side of the pier and is characterized by a strong vertical velocity component that directs the flow downwards. This down-flow accelerates the erosion of sediment from the riverbed and carries it away from the scour hole. The velocity and strength of the down-flow are influenced by factors such as flow rate, pier geometry, and sediment characteristics.

The horseshoe vortex and down-flow are interrelated components of the local scour mechanism and contribute to the erosion and removal of sediment around bridge piers. Understanding their characteristics and dynamics is essential for predicting and mitigating local scour, as well as designing stable bridge foundations. Engineers use various methods, such as physical and numerical modeling, to study and analyze the effects of the horseshoe

vortex and down-flow on scour processes and develop effective scour countermeasures where necessary.

Due to the similar flow structures of airflow around circular bodies in wind tunnels, the basic research concerns flow visualization in aerodynamics. The main flow features involve a vertically deflected flow along the circular pier model front, a horseshoe vortex system upstream of the circular pier model, a flow separation beside the circular pier model and a wake zone downstream of it shown in Fig. 1.4, for all flow conditions a horseshoe vortex system consisting of at least two vortices.

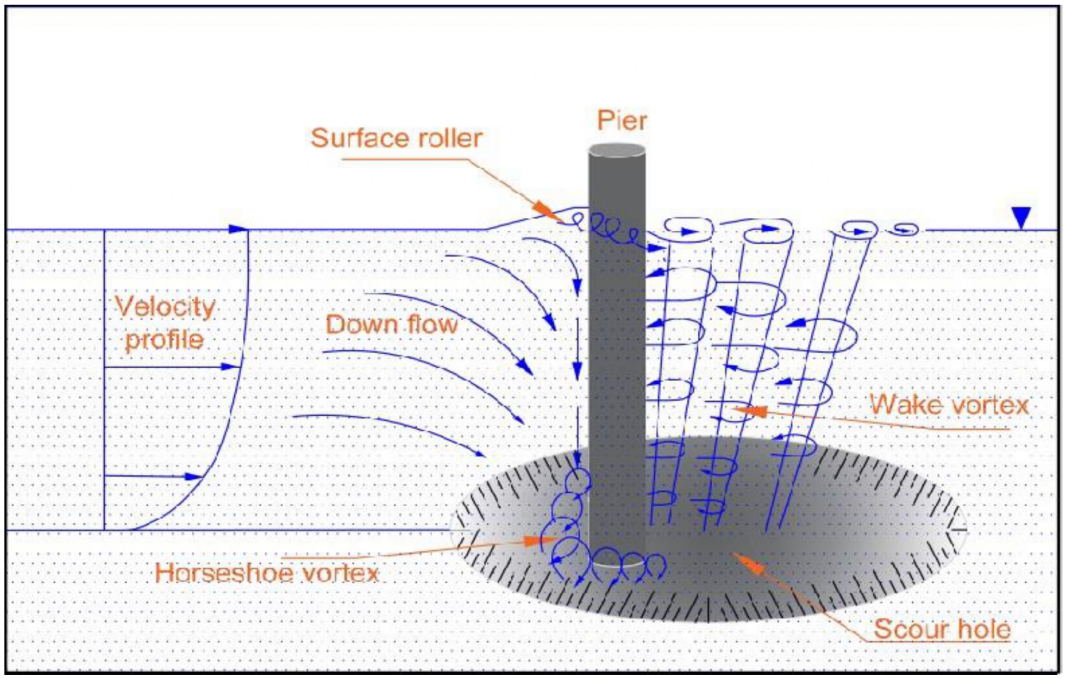


Fig 1.4 Mechanism of horseshoe vortex (Sharabian et al., 1999).

The horseshoe vortex in front of the pier is the prime agent causing scour as said by Kothyari *et al.* (1992) assuming a layer-by-layer scouring process as said by Dey (1999). Tseng *et al.* (2000) said near the upstream face of the pier there exists a down-flow which joins the separated flow to form the horseshoe vortex stretched around the pier.

1.5 Wake vortex

Wake vortices originate from flow separation at the pier's sides and develop downstream of piers. Called cast-off vortices by Raudkivi (1986), these have vertical axes. A single vortex forms on one side of sheds, and is found guilty downstream. Other forms appeared instantly on the opposite side, eventually shedding as well. As they proceed downstream, the wake vortices break up. The approach velocity and pier diameter have an inverse relationship with the frequency of vortex shedding.

Particularly little is known about wake vortex scour at bridge piers. Wake vortex scour has little to no damaging potential because it happens downstream of the pier. The horseshoe vortex scour has been extensively studied theoretically by Breusers et al. (1977)

and is well-documented with model studies by Raudkivi (1986) due to its potential to undermine the pier, which occurs near the pier's face.

Knowledge about wake vortex scour due to bridge piers has come mainly from a few laboratories' experiments. Melville (1975) stated scouring action that every concentrated vortices acts with its low-pressure centre as a vacuum cleaner. This activity picks up materials from the bed and moves them downstream.

Wake vortex scour is negligible and confluence scour is absent at most bridges. These two types of local scour can be extremely significant in clear-water rivers that move over fine sand. The opposing velocity fields at the intersection of the wake vortex streams from adjacent piers at the Tahrir and Imbaba Bridges over the Nile River in Cairo, Egypt, created the deep scour holes downstream from the enormous circular piers (10-15 m in diameter). Whereas the typical depth of flow is about 8 m, the wake vortices have caused the depths of scour to reach 8 to 11 m. In 1981 and 1987, the confluence scour, which is located where the main and side channels converge upstream from the Imbaba Bridge, measured 9 meters and was in line with the bisector of the angle at where the two channels cross. Because the bridges are located in the backwater of the Delta Barrages, the scour depths can be regarded as nearly clear-water scour, with very little sediment transport, a velocity of less than 1 m/s, and low sediment transport.

There is concern that the holes may enlarge or move upstream endangering the piers and the bridges. We have made observations in the vicinity of the scour holes and have come to the conclusion that, in each case, the scour was caused by two streams of wake vortices from adjacent piers intersecting downstream. The vortices that result from the two conflicting velocity fields create local scour. At one bridge, the scour is enhanced by the vortices that occur at the confluence of the main channel and its side channel. This is known as confluence scour.

1.6 Parameters effecting scour

1.6.1 Flow intensity

Flow intensity is defined as the ratio of the shear velocity (u^*) to the critical shear velocity (u^*_c) or the ratio of the approach mean velocity to the critical mean velocity (Melville and Chiew, 1999). Under the clear-water condition, the local scour depth in uniformly-graded sediment increases almost linearly with velocity to a maximum at the threshold velocity (Melville and Coleman, 2000). The maximum scour depth is reached when the ratio $u^*/u^*_c = 1$ and the corresponding maximum scour depth is called the threshold peak. As the velocity exceeds the threshold velocity, the local scour depth in uniform sediment first decreases and then increases again to a second peak, but the threshold peak is not exceeded provided the sediment is uniform.

1.6.2 Flow depth

The influence of flow depth on the scour depth has been discussed by many authors [e.g., Breusers and Raudkivi, 1991; Melville and Coleman, 2000). The presence of the pier in the channel causes a surface roller around the pier and a horseshoe vortex at the base of the pier. Flow depth affects local scour depth when the horseshoe vortex is affected by the formation of the surface roller (or bow wave) that forms at the leading edge of the pier. The two rollers, (i.e., the bow wave and the horseshoe vortex) rotate in opposite directions. In principle, as long as there is no interference between the two rollers, the local scour depth does not depend on the flow depth but depends only on the pier diameter.

In such a situation, which is frequently referred to as deep flow, the local scour is believed to happen at narrow piers. The surface roller becomes substantially more prominent as the flow depth drops, which reduces the horseshoe vortex's ability to entrain sediment. As a result, the local scour depth is less for shallower flows. The local scour is therefore considered to occur at a wide pier in a very shallow flow and is dependent on the flow depth.

1.6.3 Pier width

Experiments have clearly shown that it is possible to relate the scour depth to the size of the pier (Breusers et al., 1977). This observation can be explained physically by the fact that scouring is due to the horseshoe vortex system whose dimension is a function of the diameter of the pier. It has also been observed that the horseshoe vortex, being one of the main scouring agents, is proportional to the pier Reynolds number (Re), which in turn is a function of the pier diameter.

For the same value of mean approach flow velocity, therefore, the scour depth is proportional to the pier width. The influence of pier size on the local scour depth is of interest when data from the laboratory are interpreted for field use (Breusers and Raudkivi, 1991).

Under clear-water conditions, pier size influences the time taken to reach the ultimate scour depth but not its relative magnitude, if the influence of relative depth, H/D, and relative grain size D/d_{50} on the local scour depth are excluded (Breusers and Raudkivi, 1991). They also concluded that the volume of the local scour hole formed around the upstream half of the perimeter of the pier is proportional to the cube of the pier diameter (or the projected width of the pier). The larger the pier the larger the scour hole volume and also the longer the time taken for the development of the scour hole for a given shear stress ratio.

1.6.4 Pier Shape

Piers are constructed of various shapes. The most common shapes used are circular, rectangular, square, rectangular with chamfered ends, oblong, Lenticular and Joukowski. The effect of pier shape has been reported by many researchers e.g., Breusers (1977), Breusers and Raudkivi (1991), Melville and Coleman (2000).

The common consensus has been that the shallower the local scour, the blunter the pier. The maximum scour depth is found to be unaffected by the geometry of the downstream end of the pier. A form factor is frequently used to account for the pier shape.

The shape parameters for uniform piers, or piers with constant sections throughout their depth, were discussed by Melville and Chiew (1999). The anticipated width (140 mm) of the local scour depths for various pier forms is the same. According to his findings, a rectangular pier with blunt ends created the greatest scour, while a circular pier produced the least.

For piers tapered on the upstream and downstream faces, the slope, in elevation, of the leading edge of the pier affects the local scour depth. Downward-tapered piers induce deeper scour than does a circular pier of the same width.

1.6.5 Sediment Size

The effects of the grain size and the density of the sediment material are often expressed as a function of the critical flow velocity for the initiation of sediment motion. Breusers and Raudkivi (1991) reported on the work of Raudkivi and Ettema (1977) in which the effect of sediment size on the local depth of scour at a bridge pier was studied. The experiments were conducted under clear-water conditions and using a pier of diameter 7 cm and a flume 1.5 m in width. It was observed that a sediment size of $d_{50} \leq 0.7$ mm leads to the formation of ripples, whereas a sediment size of $d_{50} \geq 0.7$ mm does not cause ripples. It was further stated that the results for grain sizes which lead to the formation of ripples ($d_{50} \leq 0.7$ mm) were different from those for larger grain sizes for which ripples do not form ($d_{50} \geq 0.7$ mm).
According to Raudkivi and Ettema (1996), for non-ripple forming sediments ($d_{50} \geq 0.7$ mm), experiments can be run successfully with a flow condition, $u^* \sim 0.95\, u_{*c}$, without the upstream bed being disturbed by the approach flow, whereas with finer sands ($d_{50} < 0.7$ mm) a flatbed cannot be maintained for the same flow condition. Therefore, if the sediment is uniform sand with grain size $d_{50} < 0.7$ mm, a flatbed cannot be maintained near the threshold shear stress condition because ripples will develop, with a small amount of general sediment transport taking place so as to replenish some of the sand scoured at the pier. Thus, true clear-water scour conditions cannot be maintained for this case.

1.6.6 Flow Froude Number

A Froude number is a dimensionless number comparing inertia and gravitational forces. It may be used to quantify the resistance of an object moving through water and compare objects of different sizes. Named after William Froude, the Froude number is based on the speed/length ratio as defined by him.

$$\mathrm{Fr} = \frac{U_\infty}{\sqrt{gH}} \tag{1.1}$$

where, U_∞ is a characteristic velocity and for rectangular cross-sections with uniform depth H, For Fr < 1 the flow is called a subcritical flow, further for Fr > 1 the flow is characterized as supercritical flow. When Fr ≈ 1, the flow is denoted as critical flow.

1.6.7 Angle of repose

Granular materials have an engineering characteristic known as the angle of repose or angle of friction. The maximum angle of a stable slope is known as the angle of repose, and it depends on particle shapes, cohesion, and friction. Conical piles will form when large amounts of granular materials are placed over a horizontal surface. The angle of repose also referred to as the internal angle between the pile's surface and the horizontal surface, is influenced by the material's density, surface area, and coefficient of friction. In comparison to material with a high angle of repose, the low angle of repose material generates flatter piles. The angle of repose, then, is the angle that a pile makes with the ground.

The sharpest angle that a mass of loose particulate matter's surface can make with the ground is known as the angle of repose. The size, mass, angularity, wetness, and force of downward acceleration all have an impact on the angle of repose, yet it is constant for a particular material. For engineers and landscapers, for instance, it is crucial to understand the angle of repose of material under varied conditions.

Sand castles are the most common manner in that most people are familiar with the angle of repose. Sand that has been piled dry typically has an angle of repose of around 30°, resulting in shallow inverted cones. Sand can be used to create walls, towers, and sea caves by dampening it. This causes the surface tension of the water to bind the sand grains together and raises the angle of repose above vertical. The angle of repose is reduced to almost nil when sand is overly wet because the water lubricates the granules rather than binding them together. Anyone who is considering purchasing a home that is situated on a sandbar should have this knowledge.

1.7 CFD Modelling

CFD, or computational fluid dynamics, is a powerful tool used in various fields, including engineering, physics, and mathematics, to simulate and analyze the behavior of fluid flows. The technique involves the use of numerical methods and algorithms to solve the governing equations of fluid dynamics, converting them into a system of equations that can be solved using a computer. CFD has been widely applied to solve complex problems, such as fluid-structure interaction, turbulent flow, and multiphase flow, which are difficult or impossible to tackle with traditional analytical methods.

One of the main advantages of CFD is its capability to provide detailed and quantitative results that may not be accessible through experimental methods. Additionally, CFD simulations can allow for parametric studies, where specific design variables or input parameters can be altered to study their effects on the fluid flow and scour process. This feature is crucial in identifying optimal bridge designs and scour protection methods.

However, it's crucial to note that accurate and reliable CFD simulations require careful consideration of several factors, including the choice of numerical methods, modeling assumptions, and boundary conditions. It's essential to have a good understanding of the physical phenomena being studied and validate the CFD simulations with experimental data whenever possible. Overall, CFD can be a useful tool for investigating local scour around bridge structures and designing effective scour countermeasures.

1.7.1 Mathematical Formulation

CFD relies on fundamental equations that govern fluid flow, primarily the Navier-Stokes equations. These equations describe the conservation of mass, momentum, and energy within a fluid. Depending on the nature of the flow (incompressible or compressible), different forms of the equations are used.

1.7.2 Discretization

The continuous governing equations are transformed into discrete forms using numerical methods. This involves dividing the fluid domain into a mesh of smaller elements (cells) and approximating the derivatives in the equations using finite difference, finite volume, or finite element methods.

1.7.3 Mesh Generation

Meshing is a critical step that influences the accuracy and efficiency of the simulation. The domain is divided into a grid of cells, and the choice of mesh type (structured or unstructured) and cell shape affects how well the solution can capture complex flow features.

1.7.4 Boundary Conditions

Boundary conditions define how the fluid interacts with the domain boundaries. These conditions can include specifying inlet and outlet velocities, pressures, temperatures, and other relevant properties. Accurate boundary conditions are crucial for obtaining physically realistic results.

1.7.5 Solver Selection

Various numerical solvers are available for solving the discretized equations. The choice of solver depends on factors such as the type of flow (steady-state or transient), the presence of turbulence, and the computational resources available.

1.7.6 Solution Process

The numerical solver iteratively computes the flow field variables (velocity, pressure, temperature, etc.) on the mesh. The process continues until a convergence criterion is met, ensuring that the solution stabilizes and no further changes occur.

1.7.7 Turbulence Modeling

Turbulence is a complex and chaotic phenomenon in fluid flows. CFD simulations often use turbulence models to account for the effects of turbulence on the flow. These models

approximate turbulent behavior and are classified into various categories based on their complexity and applicability.

1.7.8 Post-Processing and Visualization

After obtaining the simulation results, post-processing techniques are used to analyze and interpret the data. Visualization tools create contour plots, vector plots, streamlines, and animations that illustrate flow patterns, pressure distribution, heat transfer, and more.

1.7.9 Validation and Verification

CFD results should be validated by comparing them to experimental data or analytical solutions. Verification involves ensuring the correctness of the numerical implementation, while validation assesses the model's accuracy in representing real-world phenomena.

1.7.10 Applications and Benefits

CFD is applied in various industries for design optimization, performance analysis, and problem-solving. It helps engineers and scientists understand fluid behavior in intricate detail, leading to improved product designs, reduced development costs, and enhanced safety.

1.7.11 Challenges and Considerations

While CFD offers powerful insights, it comes with challenges such as mesh generation difficulties, turbulence modeling uncertainties, and the need for computational resources. Careful consideration of modeling assumptions and validation processes is crucial.
In summary, Computational Fluid Dynamics is a multidisciplinary field that combines mathematics, physics, numerical methods, and computer science to simulate and analyze fluid flows. It's an indispensable tool for engineers and researchers seeking to understand complex fluid behavior and make informed decisions in various applications.

1.8 ANSYS Fluent

ANSYS Fluent is a computational fluid dynamics (CFD) software package developed by ANSYS, Inc. It is widely used by engineers and researchers to simulate and analyze fluid flow, heat transfer, and related phenomena in a wide range of industries and research institutions. Here we have particularly used fluent because Fluent can simulate various types of fluid flow, including laminar and turbulent flow, compressible and incompressible flow, multiphase flow, and non-Newtonian flow. Computational fluid dynamics (CFD) is a mathematical tool based on computer programming. The growing interest in the field of CFD based simulations has been widely used by engineers in all those areas where experimental or numerical analysis becomes cumbersome. Determination of the movement of fluid in detail by solving a system set of nonlinear governing equations after the use of specified boundary conditions over the ambit of interest is the basic principle which is used

in the analysis of CFD problems. The simulations based on CFD are contingent upon combined numerical accuracy, cost of computations and precision of modeling.
Using Ansys CFD, virtually, the system of fluid flow can be simulated using computer analysis. Analysis can be started by first of all creating a mathematical model of the physics problem associated. The CFD method of solving entails three approaches:

- Finite Difference Method
- Finite Element Method
- Finite Volume Method

1.9 Governing equations

For all the simulation strategies for the turbulent flows, whether it's the DNS or URANS method, the Navier-Stokes equations are the fundamental part. For the undertaken research, the incompressible time-dependent Navier-Stokes equation is considered along with the conservation of mass to describe the flow for the spatial domain, as given below in Eqs. (1.2-1.3).
Mass conservation: continuity equation

$$\frac{\partial u_i}{\partial x_i} = 0 \tag{1.2}$$

Momentum conservation: Navier-Stokes equations

$$\frac{\partial u_i}{\partial t} + \frac{\partial u_i u_j}{\partial x_j} = -\frac{1}{\rho}\frac{\partial P}{\partial x_i} + \nu \frac{\partial^2 u_i}{\partial x_i \partial x_j} \tag{1.3}$$

where, u_i and u_j are the velocity vector components in the corresponding direction, P is the pressure, ρ is the fluid density, and υ is the kinematic molecular viscosity.

1.10 Unsteady Reynolds-Averaged Navier-Stokes (URANS)

The Unsteady Reynolds-Averaged Navier-Stokes (URANS) model is a computational fluid dynamics (CFD) approach used to simulate fluid flow. It combines the Reynolds-Averaged Navier-Stokes (RANS) equations with time-dependent terms to capture unsteady or transient flow phenomena. RANS equations average the Navier-Stokes equations over time to simplify the simulation of turbulent flows by separating the flow into mean and fluctuating components. The resulting equations focus on the mean flow but introduce additional terms to account for turbulence, requiring a turbulence model to close the equations. Unlike RANS, which focuses on steady-state or statistically steady flows, URANS incorporates time-dependent terms to account for transient phenomena. This approach is useful for flows where unsteadiness is important, such as vortex shedding, flow separation, or interactions with moving boundaries. URANS typically uses the same turbulence models as RANS, such as the k-ε, k-ω, or Reynolds Stress Models (RSM). These models help represent the effects of turbulence on the mean flow.

In the RANS, the spatially filtered 3D time-dependent Navier-Stokes equations are solved numerically with a scale larger than the mesh size of the chosen numerical grid, while the other mainly dissipative motions are simulated by the SGS model.

The subgrid-scale stresses resulting from the filtering operation are unknown and require modelling. The subgrid-scale turbulence models usually employ the Boussinesq hypothesis (Hinze, 1975), and calculate the SGS stress τ_{ij} using the:

$$\tau_{ij} - \frac{1}{3}\tau_{kk}\delta_{ij} = 2\mu_t \bar{S}_{ij} \tag{1.4}$$

where μ_t is the subgrid-scale turbulent viscosity. τ_{kk} is the isotropic part of the subgrid-scale stresses. $\bar{S}_{ij}$ is the rate-of-strain tensor for the resolved scale defined by:

$$\bar{S}_{ij} = \frac{1}{2}\left(\frac{\partial \bar{u}_i}{\partial x_j} + \frac{\partial \bar{u}_j}{\partial x_i}\right) \tag{1.5}$$

The simple subgrid-scale-model was first proposed by Smagorinsky (1963). In the Smagorinsky-Lilly model, the eddy-viscosity is modelled by:

$$\mu_t = \rho L_s^2 \left|\bar{S}\right| \tag{1.6}$$

where L_s is the mixing length for subgrid scales and $\left|\bar{S}\right| \equiv \sqrt{2\bar{S}_{ij}\bar{S}_{ij}}$. L_s is computed using:

$$L_s = \min(K, d, C_s\Delta) \tag{1.7}$$

where K is the von Karman constant, d is the distance to the closest wall, C_s is the Smagorinsky constant, and Δ is the local grid scale. Δ is computed according to the volume of the computational cell using:

$$\Delta = V^{\frac{1}{3}} \tag{1.8}$$

Lilly derived a value of 0.17 for C_s for homogeneous isotropic turbulence in the inertial sub-range. However, this value was found to cause excessive damping of large-scale fluctuations in the presence of mean shear and in transitional flows near a solid boundary. It has to be reduced in such regions. In other words, C_s is not a universal constant, which is the most serious vital of this simple model. Nonetheless, a C_s value of around 0.1 has been found to yield the best results for a wide range of flows.

In this study, the sub-grid-scale eddy viscosity μ_t is computed using the dynamic Smagorinsky model proposed by Germano et al. (1991) and modified by Lilly (1992). In this model, the coefficient C_s is computed dynamically based on the information provided by the resolved scales of motion. The dynamic procedure thus obviates the need for users to specify the model constant C_s in advance. The C_s obtained using the dynamic Smagorinsky-Lilly model vary in time and space over a fairly wide range. To avoid numerical instability, C_s is clipped between zero and 0.23.

1.11 Eulerian Multiphase Model and *k- ε* Turbulence Model

The k-epsilon turbulence model is a widely employed approach in computational fluid dynamics (CFD) simulations to predict turbulent flow behaviors in various engineering

applications. It falls under the category of two-equation turbulence models, aiming to describe the evolution of two key turbulence quantities: turbulence kinetic energy (k) and turbulence dissipation rate (ε). This model provides a balance between computational efficiency and accuracy in capturing turbulence characteristics.

The k-epsilon turbulence model is based on a set of transport equations for turbulence kinetic energy (k) and turbulence dissipation rate (ε). These equations govern how these quantities change with respect to time and space within a turbulent flow.

1.11.1 Transport Equations for the Standard k- ε Model

The turbulence kinetic energy, k, and its rate of dissipation, ε, are obtained from the following transport equations:

$$\frac{\partial}{\partial t}(\rho k)+\frac{\partial}{\partial x_i}(\rho k u_i)=\frac{\partial}{\partial x_j}[(\mu+\frac{\mu_t}{\sigma_k})\frac{\partial k}{\partial x_j}]+G_k+G_b-\rho\varepsilon-Y_M+S_k \tag{1.9}$$

and

$$\frac{\partial}{\partial t}(\rho \varepsilon)+\frac{\partial}{\partial x_i}(\rho \varepsilon u_i)=\frac{\partial}{\partial x_j}[(\mu+\frac{\mu_t}{\sigma_\varepsilon})\frac{\partial \varepsilon}{\partial x_j}]+C_{1\varepsilon}\frac{\varepsilon}{k}(G_k+C_{3\varepsilon}G_b)-C_{2\varepsilon}\rho\frac{\varepsilon^2}{k}+S_\varepsilon \tag{1.10}$$

The term G_k, representing the production of turbulence kinetic energy, is modeled identically for the standard, RNG, and realizable k- ε models. From the exact equation for the transport of k, this term may be defined as

$$G_k=-\rho\overline{u_i'u_j'}\frac{\partial u_j}{\partial x_i} \tag{1.11}$$

To evaluate G_k in a manner consistent with the Boussinesq hypothesis,

$$G_k=\mu_t S^2 \tag{1.12}$$

where S is the modulus of the mean rate-of-strain tensor, defined as

$$S=\sqrt{2S_{ij}S_{ij}} \tag{1.13}$$

The generation of turbulence due to buoyancy is given by

$$G_b=\beta g_i\frac{\mu_t}{\mathrm{Pr}_t}\frac{\partial T}{\partial x_i} \tag{1.14}$$

where Pr_t is the turbulent Prandtl number for energy and g_i is the component of the gravitational vector in the ith direction. For the standard and realizable k- ε models, the default value of Pr_t is 0.85.

The coefficient of thermal expansion, β, is defined as

$$\beta=-\frac{1}{\rho}\left(\frac{\partial\rho}{\partial T}\right)_p \tag{1.15}$$

Y_M represents the contribution of the fluctuating dilatation in compressible turbulence to the overall dissipation rate, calculated as

$$Y_M=2\rho\varepsilon M_t^2 \tag{1.16}$$

where M_t is the turbulent Mach number defined as $M_t = \sqrt{\frac{k}{a^2}}$

where $a \equiv \sqrt{\gamma RT}$ is the speed of the sound.

$C_{1\varepsilon}$, $C_{2\varepsilon}$, and $C_{3\varepsilon}$ are constants. σ_k and σ_ε are the turbulent Prandtl numbers for k and ε, respectively. S_k and S_ε are user-defined source terms.

1.12 Modeling the Turbulent Viscosity

The turbulent (or eddy) viscosity μ_t is computed by combining k and ε as follows:

$$\mu_t = \rho C_\mu \frac{k^2}{\varepsilon} \tag{1.17}$$

where C_μ is a constant.

1.13 Model Constants

The model constants $C_{1\varepsilon}$, $C_{2\varepsilon}$, C_μ, σ_k and σ_ε have the following default values:
$C_{1\varepsilon}$=1.44, $C_{2\varepsilon}$=1.92, C_μ=0.09, σ_k=1.0, and σ_ε=1.3

These default values have been determined from experiments with air and water for fundamental turbulent shear flows including homogeneous shear flows and decaying isotropic grid turbulence. They have been found to work fairly well for a wide range of wall-bounded and free-shear flows.

1.14 Vortex shedding and Strouhal number

Since considering the flow upstream of the circular pier model, it is useful to evaluate the model predictions downstream of the circular pier model. Flow past an obstacle can result in vortices forming and shedding in the wake region. An important evaluation of the model is to consider if the phenomena are simulated appropriately.

The Strouhal number (S_t) is a dimensionless parameter which describes the shedding behaviour of the vortices in the wake region of a flow:

$$S_t = \frac{f_s D}{U_\infty} \tag{1.18}$$

where D is the diameter of the circular pier model and U_∞ is the mean velocity of the flow, f_s is the shedding frequency of the vortices equal to 1/ T_1, where T_1 denotes for period of one complete vortex shedding.

1.15 Pressure coefficient

The pressure coefficient C_p calculated using Equation-

$$C_p = \frac{(p - p_o)}{(0.5\rho U_\infty^2)} \tag{1.19}$$

where p is the local pressure at a point along the flow direction, p_o is upstream static pressure and U_∞ upstream approaching flow velocity.

1.16 Dynamics of the horseshoe vortex and scour mechanisms

To understand the complex instability mechanism that occurs upstream of the circular pier model the 3D dynamics of the vortices are studied. The 3D coherent dynamics of the horseshoe vortex system are identified using the Q criterion. This is considered an effective vortex indicator in wall turbulence and it helps to visualize the instantaneous resolved flow fields and study the resulting coherent structures of the horseshoe vortex system around the cylindrical pier.

The Q criterion is used to visualize the vortices, where Q is the second invariant of the velocity gradient tensor with dimension of (S^{-2}).

$$Q = C_Q\left(\Omega^2 - S^2\right) \tag{1.20}$$

where the constant C_Q= 0.25 in ANSYS CFD-Post. In this definition, S is the absolute value of the Strain Rate which is mentioned in Eq. (1.12), and Ω is the absolute value of vorticity, as shown below:

$$\Omega = \sqrt{2\omega_{ij}\omega_{ij}} \tag{1.21}$$

$$S_{ij} = \frac{1}{2}\left(\frac{\partial u_i}{\partial x_j} + \frac{\partial u_j}{\partial x_i}\right) \tag{1.22}$$

$$\omega_{ij} = \frac{1}{2}\left(\frac{\partial u_i}{\partial x_j} - \frac{\partial u_j}{\partial x_i}\right) \tag{1.23}$$

The reason behind this definition is to quantify vortices without mean shear rate in order to avoid displaying the steady shear layer (where, $S = \Omega = \frac{1}{2}\left|\frac{du}{dy}\right|$) (Menter, 2012).

1.17 Sediment transport modelling

In addition to the hydrodynamic flow behaviour, sediment transportation is considered a significant parameter that should be precisely modelled in a scour simulation. The scouring depth and sediment transport rate depend to a great extent on the energy and size of the horseshoe vortex which moves and interacts with the hole created by the scour evolution. As such, using the RAND in a CFD model to investigate the horseshoe vortex near the bridge piers enables an accurate representation and prediction of the depth and shape of the hole that develops during the scour process.

The sediment transport is considered to occur immediately when the bed shear stress, (which was already calculated from the RANS), exceeds the critical shear stress of the sediment particle, (this is called the incipient motion of sediment) (Chien, 1999). After the incipient motion, the sediment transport rate becomes another key criterion to quantitatively describe the development and level of scour in real-time. Therefore, the incipient motion of sediment and sediment transport rate must first be measured as they are two key parameters that determine the quality of any sediment transport model.

1.17.1 Incipient motion of sediment

A widely used procedure to determine the incipient motion for non-cohesive particles is represented by the Shields curve (Shields, 1936), which is based on the results of numerous laboratory measurements with different grain sizes, densities and wall shear stresses. The most commonly used method to predict the sediment inception is based on the excess critical shear stress (Simões, 2014; van Rijn, 1984). The critical shear stress of sediment proposed by Shields (1936) is defined by:

$$\tau_{b.cr} = g(\rho_s - \rho)d_{50}\theta_{cr} \tag{1.24}$$

where, $\tau_{b.cr}$= critical shear stress of sediment; ρ = fluid density; ρ_s =sediment material density; d_{50} = median diameter of sediment particle; and θ_{cr}= critical Shields number (dimensionless), which is determined by:

$$\theta_{cr} = \begin{cases} 0.24D_*^{-1} & ,D_* \le 4 \\ 0.14D_*^{-0.64} & ,4<D_* \le 10 \\ 0.24D_*^{-0.10} & ,10<D_* \le 20 \\ 0.013D_*^{0.29} & ,20<D_* \le 150 \\ 0.055 & ,150 < D_* \end{cases} \tag{1.25}$$

where $D_* = d_{50}[(s-1)g/\nu^2]^{\frac{1}{3}}$; and υ = kinematic viscosity coefficient; s =relative density of the sediment particle. In reality, the riverbed is not always flat despite Equation 1.24 being designed for the flat riverbed. The formula of dimensionless critical shear stress is shown in Equation 1.26.

$$T = (\tau_b - \tau_{b.cr}) / \tau_{b.cr} \tag{1.26}$$

where T = dimensionless critical shear stress; and τ_b = shear stress of sediment. Once τ_b becomes greater than $\tau_{b.cr}$, the triggering removal value in the current sediment transport modelling, the incipient motion of sediment can take place immediately.

1.17.2 Rate of sediment transport

After the sediment movement begins, the sediment transport rate becomes another key parameter that describes the scour process. The sediment transport rate is characterized as

the movement of solid particles, both particulate and dissolved, that go over a given stream transverse cross-section of a given flow in a unit of time, and its calculation can be given by van Rijn (1986):

$$\frac{dh}{dt} = -0.00033\rho_s(\Delta g d_{50})^{0.5}\frac{D_*^{0.3}}{1-n}T^{1.5} \tag{1.27}$$

In which h = riverbed elevation; t = time; n = void ratio of sediment (which is set as 0.4 based on (Yanmaz and Altinbilek, 1991, Melville, 1997)); $\Delta = (\rho_s\text{-}\rho)/\rho$ = relative density; and T should be obtained from Equation 1.26. This equation only computes the erosion of the sediment around the bridge pier (there is no sediment deposition has been noticed around the circular pier model).

By programming Equation 1.27 in a computer language such as C^{++} and embedding it in the CFD code (ANSYS Fluent) as a UDF, the bed of the river can be updated according to the calculated shear based on the riverbed elevation (h) for each time step of the scour simulation. This way the transient variations of the riverbed elevation can be technically accounted for in real time using the CFD simulation.

Chapter 2
Literature Review

Pier scour is a complicated phenomenon. There are several reasons why scour occurs near the pier. One of the main causes is a change in the flow field brought on by a blockage in the flow. This chapter covers a survey of the literature on a number of topics related to scouring around circular uniform bridge piers and the effect of the coherent structures and horseshoe vortex system around the bridge pier on the scour depth and pattern. It also discusses the flow structure surrounding uniform and compound piers and how it changes in sections along the height; it also presents the time evolution of scour around uniform and compound bridge piers and various geometric standard deviations of the sediments.

Chabert and Engeldinger (1956) conducted twenty laboratory runs on a compound bridge pier having foundations of large circular diameters of various dimensions. They recommended a better combination to reduce the scour was a footing having a diameter three times the diameter of the pier and located at 0.4 times the pier diameter below the bed level. This will reduce the scour by one-third of that due to the pier alone.

Dargahi's (1989) experiment for fixed beds and Dargahi's (1990) experiment for mobile beds are considered the most important in this field. They investigated the flow field around a vertical circular pier model mounted on flat and mobile beds by using the Hydrogen Bubble Flow technique for various ranges of R_e (from 6.5×10^3 to 6.5×10^4). They found that the horseshoe vortices upstream of the circular pier model had a significant effect on the main flow characteristic, and the number of vortices related to R_e, and also that for each constant R_e there are different flow patterns. These two experiments are considered the only ones available for scouring around bridge piers field that relates to the horseshoe vortex system and the scour process.

Melville (1997) provided an overview of experimental research done at the University of Auckland on bridge pier and abutment scour. A consolidated approach was proposed to forecast local scour at piers and abutments. The author took into account the following factors when developing the empirical relations: kind of sediment, depth and velocity of flow, shape, size, and alignment of scour around the circular compound bridge pier foundation. An example of the design process was provided for future reference.

Chang et al. (2004) carried out investigations to determine the scour depth around circular piers in clear water conditions using different sediment combinations. They created a technique for estimating the depth of scour in sediment mixes and gathered data on the temporal evolution of scour from previous researchers. They stated that their developed model performed better and confirmed it using data from previous researchers.

Wei and Huhe (2006) investigated numerically the turbulent flow field and the scouring effect around a circular pier using the LES method with Smagorinsky's SGS turbulence model for three scouring holes (scour depth (S) to pier diameter (D) ratio = 0, 0.375 and 0.85 respectively). They found that the value of mean bed shear stress is essentially affected by the horseshoe vortices inside the scour hole. While approaching the downstream of the pier, there was a gradual reduction in bed shear stress, eventually reaching the undisturbed shear stress level as the depth of scouring increased.

Kothyari et al. (2007) suggested a strategy for the time-evolution of scour around bridge parts in the case of clear water. They conducted laboratory research on scour at different-shaped piers and abutments. Large amounts of data from the preceding investigations were used to validate the model they proposed. This research is beneficial for designing different elements that hinder the flow as well as for creating riprap.

Link et al. (2008) used the LES model with the dynamic Smagorinsky model, and the wall function model suggested by Werner and Wengle (1993). The geometry of the developing scour hole was provided from the experimental data at time = 6 hrs. During the simulation, the geometry was kept constant. The predicted results provide good evidence that the dynamics of the vortex system have a significant effect on the shape of the scour hole and vice versa.

Kirkil et al. (2009) used DES based on a Spalart-Allmaras RANS model to investigate the characteristics of the coherent large-scale eddies in the flow around a circular pier with an equilibrium scour hole. They studied the mechanisms of flow and turbulent structures around the cylinder and their effects on the sediment transport during the later stage of the scour process and at a high $Re=2.06 \times 10^5$ (based on the diameter of the pier).

Kardan (2012) investigated the turbulent flow and bed shear stress around and downstream of the circular bridge pier mounted on the flatbed with $Re=8.0\times10^4$. The simulation was undertaken using various turbulent flow models (k-ε, and RSMS). They found that RANS presented more accurate results for simulating the wake vortices shedding at the downstream of the bridge pier and for evaluating the vortex fluctuation and predicted bed shear stress.

Guo (2012) conducted studies utilizing non-uniform sediments to investigate pier scour in clear water conditions. The purpose of this study was to propose a useful technique for scour depth estimation that can be applied to design. After reviewing a few earlier studies, the author proposed a straightforward scour process in terms of the interactions between sediment, flow, and structure. Based on the scour process, an assumption was made about the equilibrium scour depth, and a model was proposed and verified using data obtained by flumes. The study's proposed model offers broad recommendations for scour depth design.

Younis and Abrishamchi (2014) predicted the unsteady flow structure around a 3D square bridge pier mounted on a flat bed at Re in the range 10^4-10^5. They used two approaches to analyse their model. The URANS method was used with the k-ε turbulence model to calculate the output Reynolds stresses to solve the model. They found that the use of URANS can produce similar predictions to those obtained with LES.

Das *et al.* (2014) conducted an experimental study of the flow pattern and characteristics of a local equilibrium scour around a set of two identically shaped equilateral triangular piers placed in the longitudinal direction of the flow with an eccentricity (transverse distance). Here, the eccentricity and longitudinal spacing were equal to three times of pier width and 0.5 times the scour-affected length in the equilibrium condition of a single pier. The maximum depth of the scour at the eccentric rear pier was about 44% greater than that in the single-pier case. In addition, the maximum depth of the scour hole at the upstream of the inline front pier was about 29% more than that in the single pier case.

Das and Mazumdar (2015) carried out an experimental study to investigate the horse-shoe vortex and flow characteristics in a local equilibrium scour hole around two identical cylindrical piers placed along the flow with an eccentricity and concluded that the eccentric arrangement of piers plays an important role in the formation of greater scour depth at the eccentric rear pier.

Das *et al.* (2015) examined the local equilibrium scour features around a set of two identical circulars, square, and triangular-shaped piers positioned in the flow's longitudinal direction with a constant eccentricity (transverse distance). The study's major goal was to investigate how the kind of scouring changed as a result of the mutual interference of one pie on another with various longitudinal distances of 0.25, 0.375, 0.5, 0.625, and 0.75 times the scour-affected lengths for a single pier experiment. The study of the results was primarily concerned with the change of specific non-dimensional equilibrium scour parameters with effective pier width.

Das *et al.* (2016) determined the equilibrium scour geometry around two circular, square, and equilateral triangular piers, positioned in in-line front and eccentric rear arrangement, which is determined by carrying out 19 clear water scour tests. Here the eccentricity was kept constant with the varying longitudinal spacing (l) from 0.25, 0.375, 0.5, 0.625, and 0.75 times the maximum equilibrium scour-affected length for a single-pier test (L). At $l = 0.75L$, the maximum scour depth at the eccentric rear pier is found about 45–60% greater than that in the single-pier case. In addition, at l equal to $0.75L$, the maximum depth of the scour hole at the upstream of the in-line front pier is about 35% more than that in the single-pier case.

Wen *et al.* (2016) proposed a three-dimensional bridge scour model using the Eulerian multiphase model. Water is used as the primary phase and sediments are treated as the secondary phase. They also investigated the three-dimensional scour models for single-phase flow using water as the only phase and compared it with the multiphase model. During the model development process, they first examined the basic conservation equations and four unique simulation issues. The four simulation challenges are numerically solved and examined. Moreover, the single-phase and two-phase models are solved and analyzed. The two-phase flow model for bridge scour is more accurate as compared to single phase model for safe and long-term bridge designs in various river environments. They concluded that by optimizing the pier shapes or geometry, local scouring near the pier toe can be reduced.

Zaid *et al.* (2016) used the CFD technique to simulate the 3D flow and local scouring around bridge piers. Navier-Stokes equations are solved with the finite difference method with the RNG k-SST turbulence model. The volume of fluid (VOF) technique is used to analyze the free water surface. They used six different shapes of bridge piers namely rectangular, oblong, elliptical, sharp nose, hexagonal and streamlined. Scour depth and velocity distribution are measured on the bed surface both in numerical and experimental models. The results showed that there is an error range from (5.1%-9.8%) and (1.8%-6.1%) for prediction scour depth and maximum velocity respectively. The velocity distribution and scour depth calculations are conducted based on previous laboratory experiments.

Prasanna and Kumar (2018) investigated the flow behavior and the scour phenomenon around the bridge piers. Moreover, the numerical simulations were even

computed using CFD- Fluent, k-ε turbulence model, to elaborate the physics behind the scour formation. In the present study, scour depth was estimated making use of well-known empirical formulae. Further, it was also determined experimentally for two plan shapes of bridge piers viz., circular and oblong. The experimental results were in good consonance with the empirical formulae. The simulation results for dynamic and static pressures along with the velocity magnitude profiles, showed good similarities with the experimental results. Hence, the CFD simulation tool can be used for a wide understanding of the flow behavior around the bridge piers even without physical model studies.

Guan et al. (2019) made an attempt to estimate the turbulent flow field in a developing scour hole under clear water conditions around a circular pier. They used the technique of particle image velocimetry. They found that during the scour advancement, the horseshoe vortex system was developing from a very small vortex to three vortices. They also found that the size and strength of the main vortex increase with the increase in scour depth. These investigations provide novel information about complex flow sediment interaction.

Das *et al.* (2019) investigated the relative scour situation near three pier groupings. The scour geometries were shown when two tandem piers are placed in line with one another and a third pier is placed eccentrically in the middle of the tandem piers. Laboratory scale experiments were physically performed by gradually varying the intermediate longitudinal spacing between tandem piers. After each experimental run, the scour formation around the pier group and the dune formation downstream of the pier group are investigated.

Karimi *et al.* (2020) This study addresses the effectiveness of collars on scouring reduction around abutments and pier bridges. The different aspects of interactions between collars with abutments and piers scouring phenomena were discussed in this paper. The purpose was to study the effects of different sizes of collars on a rectangular abutment and their location to the surface of the sedimentary abutment on bridge group piers scour reduction in the presence of debris.

Terrance Charles *et al.* (2021) analysed the flow around 2D and 3D tandem bluff bodies has been carried out to investigate the influence of the gap spacing on the flow field, especially to improve the current understanding of why there is a sudden change in the downstream body drag in the 2D case at a critical gap spacing whereas such change is gradual in the 3D case. The RANS approach was used in his study.

Chen *et al.* (2022) conducted three-dimensional direct numerical simulations of flow past two stationary side-by-side circular cylinders. The effects of the three-dimensional vortical structures on the hydrodynamic forces and flow behaviours were studied associated with the cylinder length effects and underlying mechanism for the switching behavior of the gap flow.

From the literature review, it is observed that many researchers have carried out investigations considering various shapes of the pier and recommended relationships for the estimation of scour around it. Mostly, studies reported using uniform and non-uniform sediment in the case of the uniform circular pier. It has been observed that changes in footing size and pier shape have considerable influence on scour and time evolution of scour around bridge foundations. The scour depth is mostly dependent on the depth of footing

with respect to the channel bed level. Hence, there is an urgent need to carry out investigations on flow characteristics with the help of different mathematical models like k-ε and k-ω under the CFD analysis tool.

Chapter 3
Objectives and Methodology

3.1 Objectives

The aim of this study is to use CFD with the incorporation of URANS (Unsteady Reynolds Averaged Navier–Stokes) to accurately simulate and identify the detail of the flow structures that cause scour, in particular, the horseshoe and wake vortices over the entire three-dimensional flow field around bridge piers during the initial stage of the scour process.

The objective is to study the turbulent flow structure around a circular cylindrical bridge pier mounted on a fixed flat bed in a straight flow channel. A URANS will be employed in the simulation to provide details of the turbulent structure of the flow. The results are compared with other Reynolds Averaged Navier–Stokes (RANS) methods such as k-ε standard and k-ω SST, and also with experimental data obtained from Dargahi's (1989) experiments.

Simulating the time-dependent scour of a circular bridge pier model located on a flat bed is performed using the RANS technique. It will simulate the effect of down-flow, horseshoe and wake vortices on the bed shear stress with respect to increasing the scour depth. The methodology used to calculate the scour depth around the pier involves moving an initial flatbed downward in increments proportional to the excess shear stress above critical, at a point on the bed.

3.2 Configuration investigated

The flow studied in this chapter was set up to correspond to the experiment conducted by Dargahi (1989) so that a comparison with experimental data is possible. The Dargahi (1989) experiments were carried out in a rectangular cross-section flume of width B = 1.5m, and water depth of H = 0.2m. A circular cylinder of 0.15m diameter was placed vertically on the flume bed along the centre line at a distance of 18m from the inlet. Sand with a mean diameter of d_{50} = 0.365 mm was placed in the flume. The R_e of the approaching flow based on the cylinder diameter was $R_p = 3.9\times10^4$. Table 3.1 lists the basic dimensions and scales considered in the investigation.

Table 3.1: Dimensions of the flow studied, with the corresponding Reynolds and Froude numbers.

U_∞ (m/s)	D (m)	B (m)	H (m)	Re	Fr
0.26	0.10	1.5	0.2	3.9×10^4	0.19

The computational domain used to simulate the turbulent flow around a single circular cylinder is given in Fig 3.1. The coordinate system used in this study is also shown. No-slip boundary conditions are applied on the bottom wall, cylinder surface, and the sidewalls of

the channel. Note that the width of the channel of interest is narrow enough to directly affect the flow features in the vicinity of the cylindrical pier. For this reason, the side walls of the channel are included in the calculation and treated as no-slip walls.

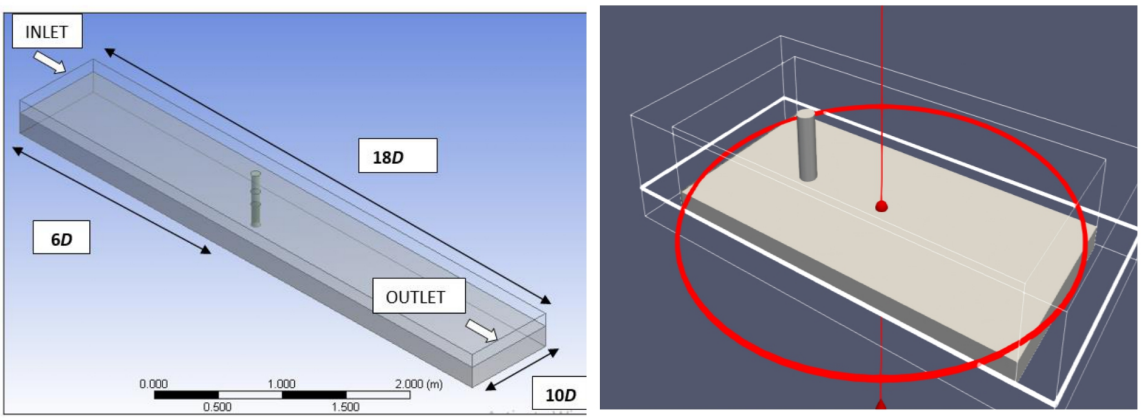


Fig 3.1 Experimental setup for numerical simulation

To study the grid size sensitivity of the solution, the computational domain has been discretised using a hexahedral grid and simulations are undertaken with computational meshes (9×10^6 and 12×10^6 grid cells) as shown in Fig. 3.2. The flow field is computed to examine whether the essential dynamics of the horseshoe vortices system can be captured with similar accuracy using different grid densities.

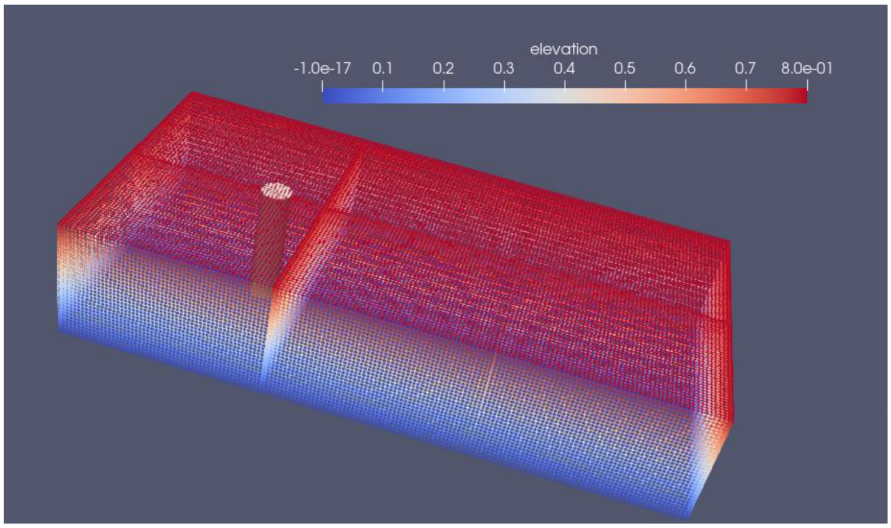


Fig 3.2 Meshing for numerical simulation

3.3 Named Selections

Named selections are being carried out for the 3-dimensional model (Fig. 3.3). The inlet is taken at the left end of the flume and the outlet is taken at the right end. The flume height is divided into two parts, the upper part is named as flow domain and the below part is taken

as the sand bed. The top surface is considered a free surface with zero shear stress conditions.

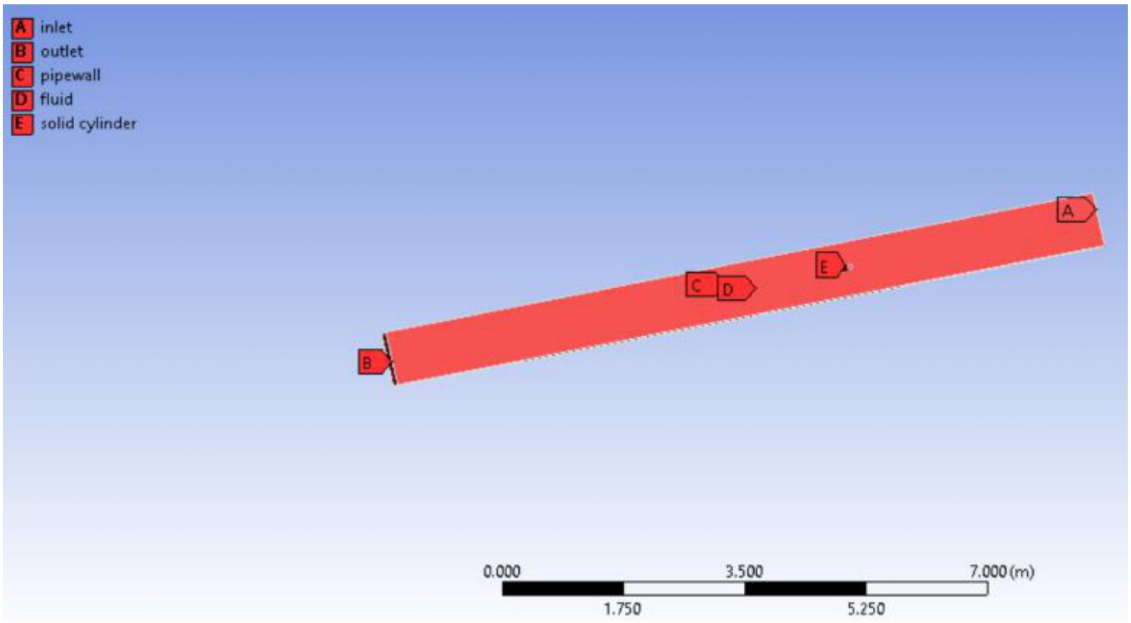


Fig 3.3 Named Selections of Geometry

3.4 Solution method

The simulations were carried out using the ANSYS Fluent CFD software. Segregated pressure solver was used to solve the spatially filtered 3D time-dependent Navier-Stokes equations. The solver uses the SIMPLE scheme for pressure-velocity coupling and a least-squares cell-based approach for gradient evaluation. The unsteady RANS employs a second-order bounded central spatial discretisation scheme along with an implicit second-order time marching scheme. The time step is calculated to keep the maximum Courant–Friedrichs–Lewy (CFL) number smaller than 1.0 for the main calculation. A maximum of 20 error-reduction sub-iterations per time step was used. Table 3.2 below represents the setup parameters used in the study for the turbulent flow around the cylinder bridge pier using RANS.

Table 3.2 CFD setup parameters

General		**Solution controls and residual monitors**	
Solver Type	Pressure-Based	**Under relaxation factor**	
Velocity Formulation	Absolute	Pressure	0.3
Time	Transient	Density	1.0
Viscous	LES	Body Force	1.0
Material		Momentum	0.7

Fluid	Water Liquid	**Convergence absolute criteria**	
Density	998.2 kg/m^3	Continuity	1×10^{-4}
Viscosity	0.001003 kg/(m. second)	x-velocity	1×10^{-4}
Solution methods		y-velocity	1×10^{-4}
Scheme	SIMPLE	z-velocity	1×10^{-4}
Spatial discretisation			
Gradient	Least Squares Cell Based		
Pressure	Standard		
Momentum	Bounded Central Differencing		
Transient Formulation	Bounded Second Order Implicit		

3.5 Boundary Conditions

As for the boundary conditions, a Drichlet-type boundary ($u=U_\infty$, $v=0$, $w=0$) was adopted at the inflow, whereas a Neumann-type boundary ($\partial u/\partial x=0$, $\partial v/\partial x=0$, $\partial w/\partial x=0$) was employed at the outflow. The top surface was free slip ($\partial u/\partial y=0$, $v=0$), while a periodic boundary condition was adopted at the cylinder ends. The no-slip boundary condition is applied on the cylinder surface and wall surface. Table 3.3 shows the boundary conditions in different sections with their initial values.

Table 3.3 Boundary Conditions

Section	Type	Initial Value
Inlet	Velocity Inlet	0.247 m/s
Outlet	Pressure Outlet	Gauge Pressure = 0
Flow Domain Sidewall	Wall	Stationary Wall with No slip condition
Pier Wall	Wall	Stationary Wall with No slip condition
Top Surface	Wall	Stationary Wall with Zero Shear Stress (Free Surface)
Sand Top	Wall	Stationary Wall with No slip condition

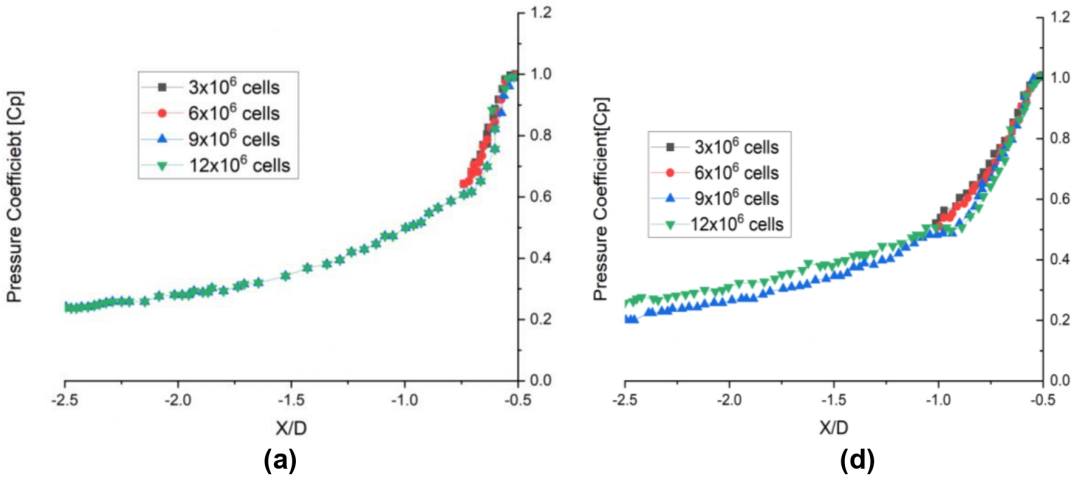
Chapter 4
Results and Discussion

4.1 Flow past a Circular Pier Model mounted on a Flat Bed

This chapter aims to demonstrate how the numerical parameters of the URANS affect the turbulent statistics and predicted time-averaged flow of the flow around a circular cylinder. The k-ε standard and *k-ω* SST URANS models are used to compare the Dargahi (1989) results. Industry applications frequently employ the k-ε standard. Nonetheless, Wilcox (2006) reports that the *k-ω* approaches have demonstrated affordable predictions for near-wall behavior in divided flow situations. On the other hand, Nieto et al. (2015) discovered that *k-ω* SST offers the ideal balance between computational expense, precision, and strength. An evaluation of the results of experimental data reported by Dargahi (1989) and two URANS methods, *k-ε* standard and *k-ω* SST will be defined.

4.1.1 Mean flow and turbulence statistics around the cylinder

The comparison of the experimental data and two different URANS methods are studied respectively. URANS approaches with *k-ε* standard and *k-ω* SST models with mesh size equal to 12×10^6 and time step equal to 0.001 seconds for unsteady flow around a circular cylinder are given. The mesh interdependency that was already carried out on these two models (*k-ε* standard and *k-ω* SST) shows that there is no significant effect on the predicted results after 9×10^6 grid size. The pressure coefficient at the bed in the symmetry plane upstream of the cylinder, the bed shear stress in the symmetry plane upstream of the cylinder, and the pressure coefficient at the stagnation point in the front face of the cylinder are shown in Fig 4.1. This section's main objective is to show how accurately the URANS model captures the complex flow around bridge piers.



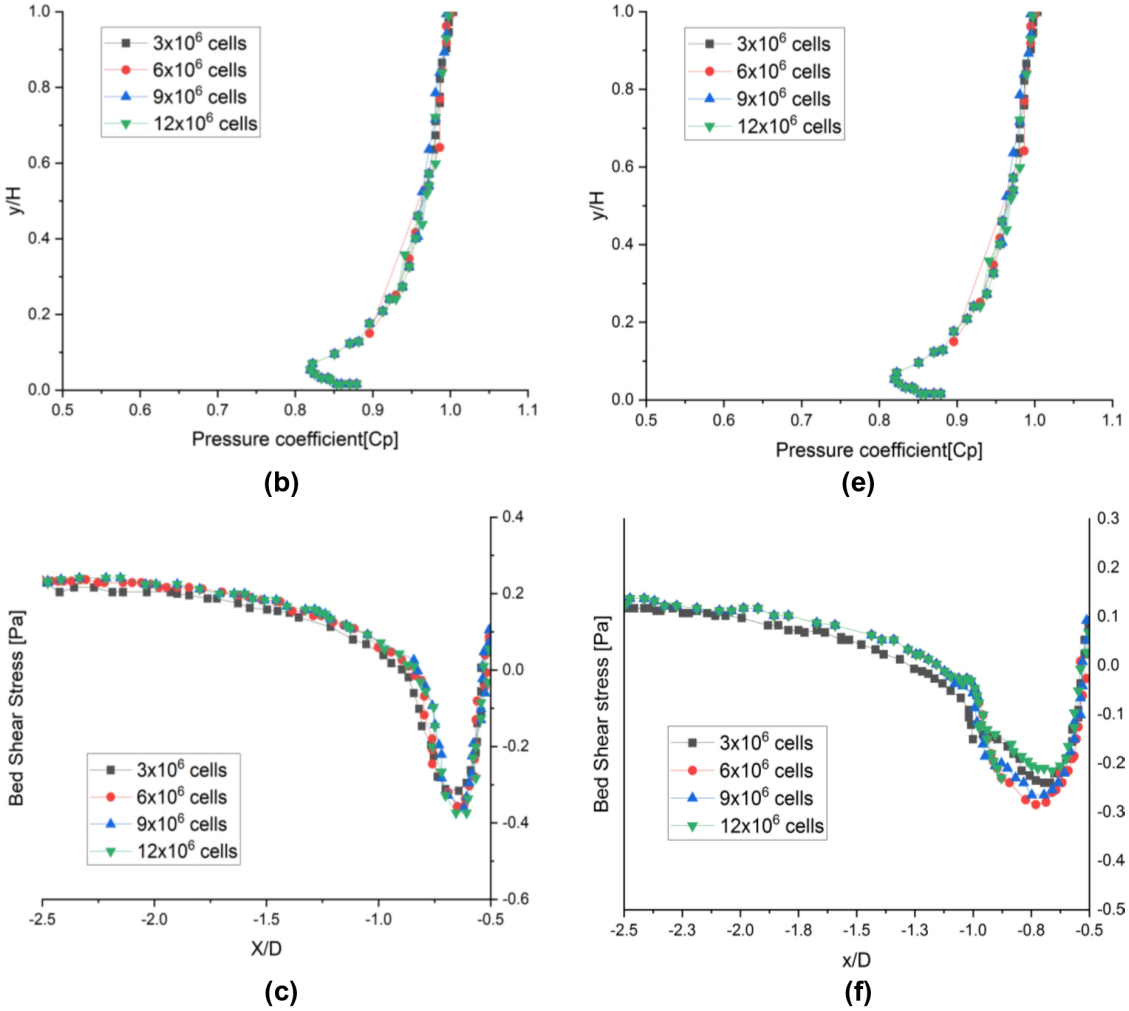


Fig 4.1 Mesh independency study for *k-ε* standard model (Fig a, b and c), and *k-ω* SST model (Fig d, e and f).

After a fully developed turbulent flow was obtained, the projected findings (i.e., velocity distribution, pressure coefficient, and wall shear stress) were averaged. It performed over 30,000 time steps to obtain flow statistics.

The findings were contrasted with the experimental findings offered by Dargahi (1989). Profiles were created using the simulation data along the symmetry plane upstream of the cylinder and along lines perpendicular to the flow direction at two heights from the channel bed in order to show the flow features (y/H=0.1 and y/H=0.95) and at several distances downstream of the cylinder as shown in Fig 4.2.

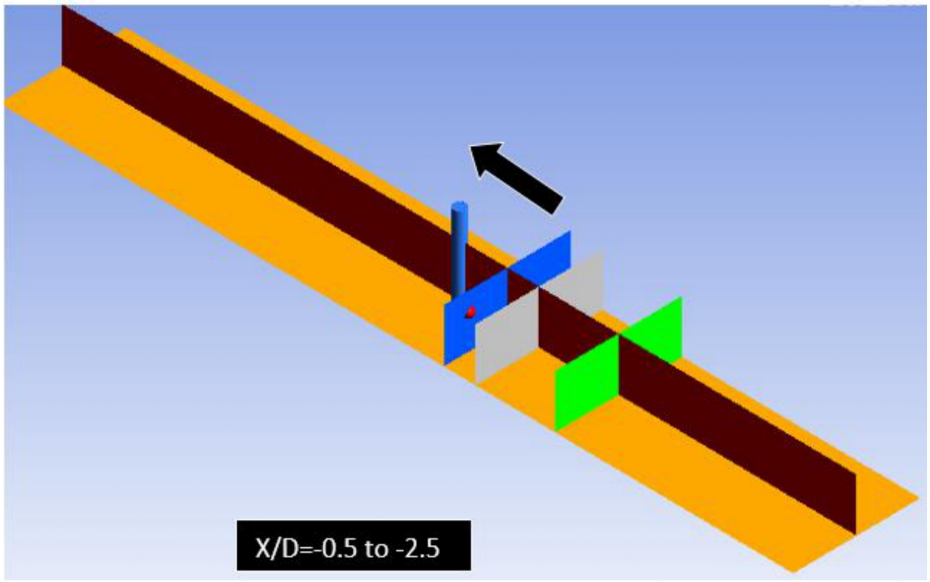
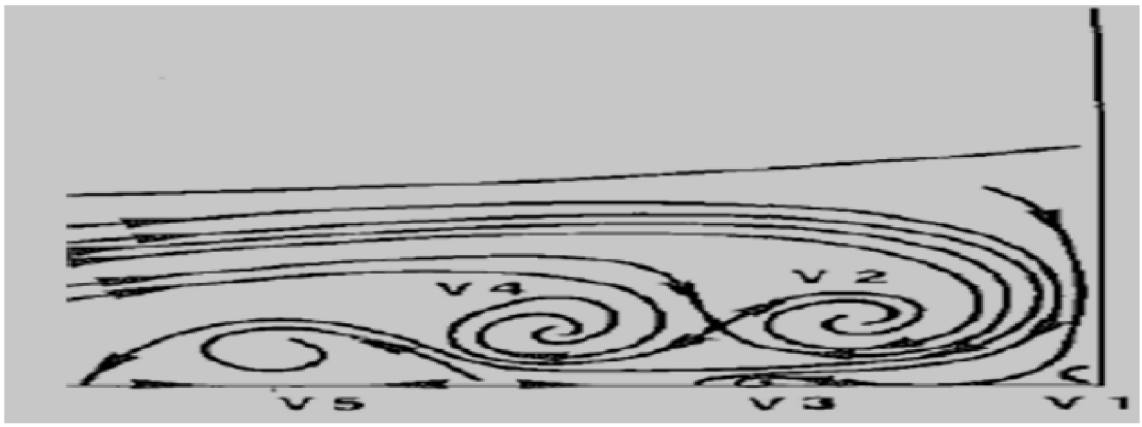


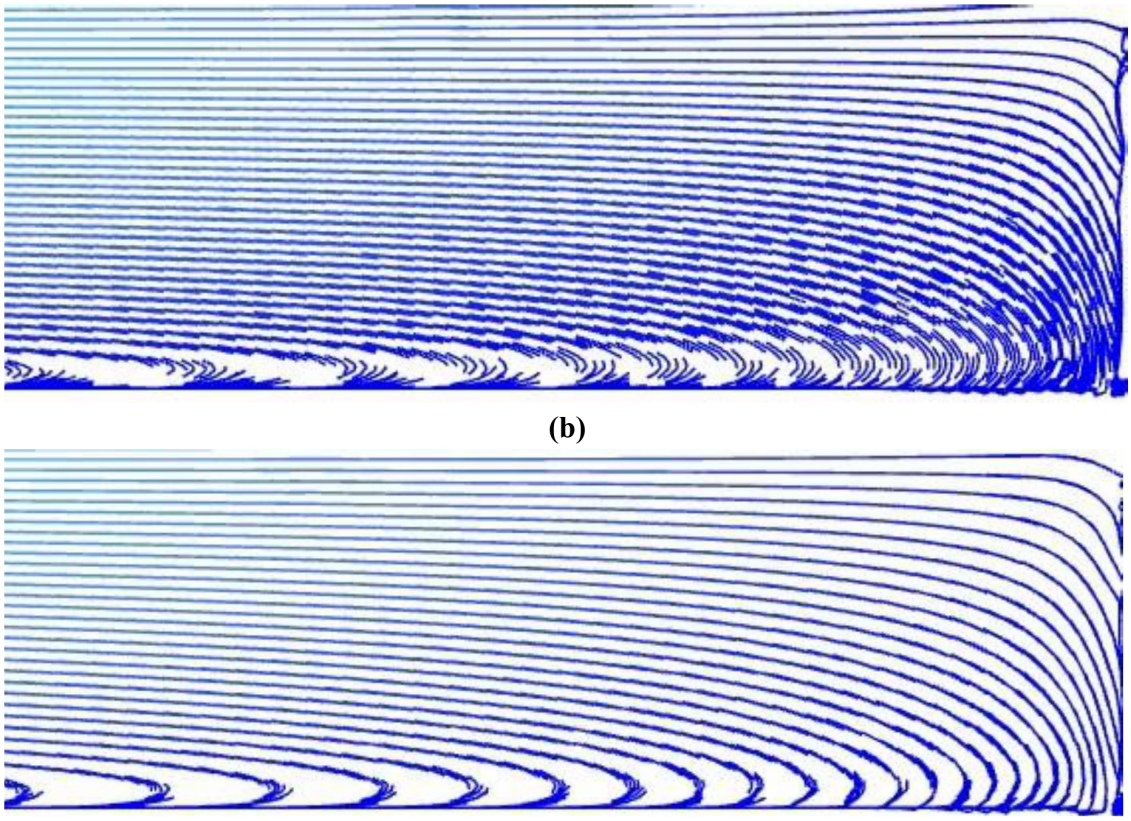
Fig 4.2 Horseshoe vortices upstream of the cylinder

Fig 4.3 (a) depicts the horseshoe vortex system architecture by Dargahi (1989) across the complete range of Re (6,600 ≤ Re ≤ 65,000), whereas Fig 4.3 (b) depicts the modelled flow field from the *k-ε* standard model in the symmetry plane. Fig 4.3 (b) displays a single obvious vortex at a distance of -0.85 times the cylinder's diameter from the center of the pier, which is in opposition to the experimental finding from Dargahi (1989). In the *k- ω* SST model, the horseshoe vortex system for the same R_e of Dargahi (1989) is shown in Fig 4.3(c).

It is evident that the horseshoe-shaped vortex system in front of the pier was made up of 5 main vortices. Two primary vortices designated *V*2 and *V*4, are separated from the center of the pier by distances of -0.8 and -0.95 times the diameter of the cylinder, respectively. Their respective secondary structures designated V3 and V5, are separated from the center of the pier by distances of 0.86 and 1.06 times the diameter of the cylinder, respectively. The corner vortex at the base of the pier designated V1, is also present in Dargahi (1989).



(a)



(b)

(c)

Fig 4.3 Instantaneous horseshoe vortex system at the symmetry plane in front of the cylinder (a) reported by Dargahi (1989), (b) *k-ε* standard model and (c) *k-ω* SST model

4.2 Vortex shedding and Strouhal number

It is important to assess the model predictions downstream of the cylinder after taking the flow upstream of the cylinder into account. Vortices may form and dissipate in the area of flow behind an obstruction. The model's ability to accurately reproduce the phenomena must be taken into consideration while making a judgment.

The vortex sheds in the cylinder's wake region with $R_p=3.9\times10^4$ is compared with the outcomes of the URANS models with the published experimental results allowing for discussion and evaluation. The URANS models are both implemented using a grid size of $12x10^6$ cells.

Table 4.1 displays the mean drag coefficient (C_d), shedding frequency (f_s), and Strouhal number (S_t) derived from the results of each turbulence model simulation so that the projected results can be compared with the experimental data that has been provided by Dargahi (1989) such as (C_d=1.15, f_s=0.32 Hz, S_t =0.185). This demonstrates that compared to experimental values, the k-Ɛ model and k-SST projected reduced C_d values.

Based on the frequency of the lift coefficient's shedding, the Strouhal number of the flow is determined. Using the Fast Fourier Transform (FFT), the lift coefficient's time domain data is transformed into its frequency domain equivalent.

The Strouhal number is then obtained from Equation 1.17 by substituting the frequency of the lift coefficient, fs. The energy dissipation away from the peck using the FFT approach is shown in Table 4.1. As anticipated and in keeping with Patel (2010), the *k-ε* model is unable to forecast the frequency of any vortex shedding, but the k-SST models are able to mimic vortex shedding.

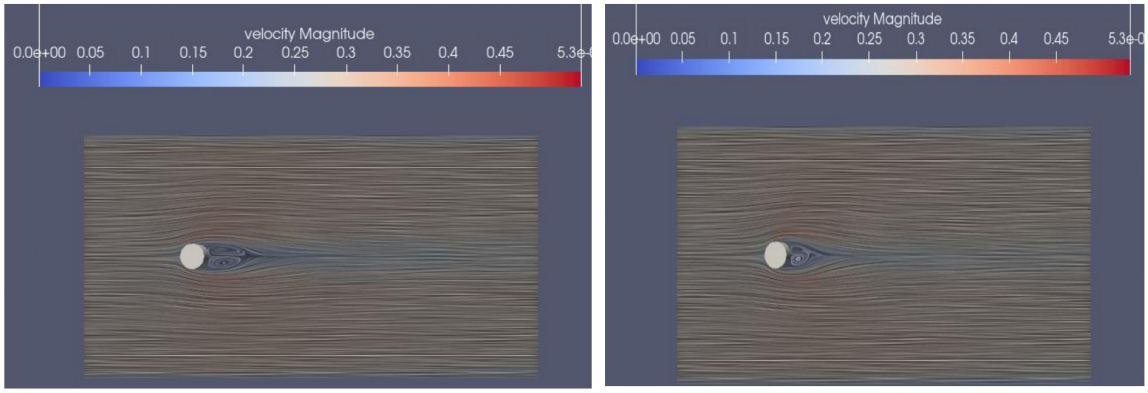
Table 4.1 Summary of predicted drag coefficient, C_d, and downstream vortex shedding parameters for circular cylinder using FFT method and visualization method.

Model	C_d	FFT method		Visualization method		Difference between the two methods
		f_s (Hz)	St	f_s (Hz)	St	
k-ε-standard	0.80	-------	------	-------	------	--------
k-ω SST	0.91	0.182	0.11	0.22	0.128	14%
Experimental Study by Dargahi (1989)	1.15	-------	-------	0.32	0.185	-------

Table 4.1 depicts the lift coefficient's spectral analysis utilizing FFT applied to anticipated flow in URANS for the flow past a circular cylinder in the Z-direction and at the channel's free surface ($y/H = 1.0$). It is obvious that the *k- ε* model is incapable of foreseeing vortex shedding, but the *k- ω* SST model somewhat overestimates it for Re.

By visualizing the frequency of the vortices being shed and plotting streamlines of the velocity field behind the cylinder for a time series, the Strouhal number and the vortex shedding frequency are also calculated.

Figure 4.4 uses the *k-ε* standard to show the velocity magnitude streamlines in the wake region of the flow through a circular cylinder. It is evident that there is certain change in the profile with regard to time from observing the velocity distribution around the cylinder for a certain flow time. As mentioned above, in Fig 4.4 the *k-ε* standard is able to capture the vortex shedding behind the cylinder.



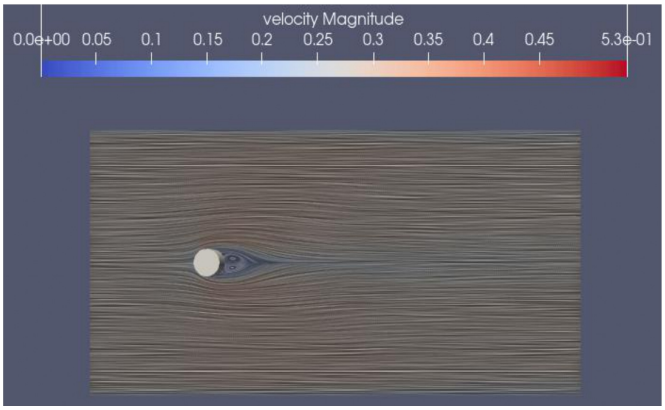
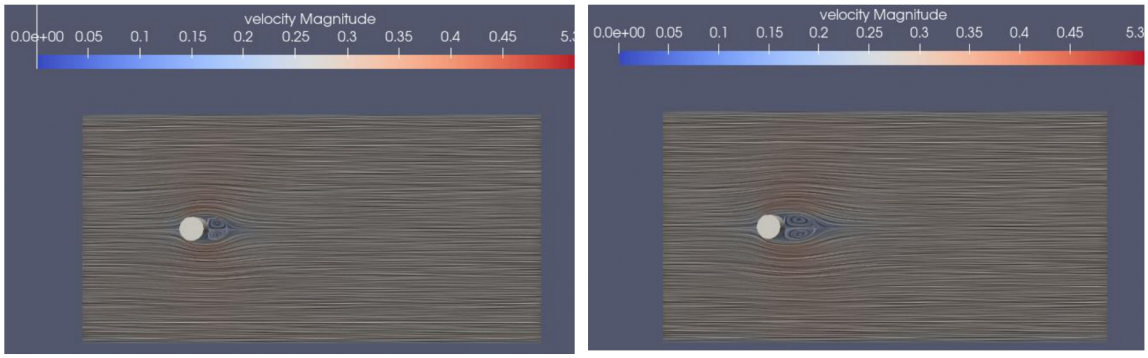


Fig 4.4 Velocity magnitude streamlines using the *k-ε* standard using 0.5 sec time step

Figure 4.5 shows the velocity magnitude streamlines for the flow behind the circular cylinder for *k-ω* SST. This demonstrates that downstream of the cylinder, the *k- ω* SST is successful in capturing vortex shedding, from which frequency may be calculated at $R_p = 3.9 \times 10^4$.

Figure 4.6 shows the velocity magnitude streamlines every 0.5 seconds in the wake region of the circular cylinder using the k-SST method. It depicts the entirety of one vortex's shedding, which takes roughly 4 seconds. This is quite near to the experimentally recorded vortex shedding frequency, which is comparable to 0.33 Hz for the frequency by Dargahi (1989).

It is evident from a comparison of the vortex shedding frequency results from the FFT approach and the visualizing method that the f_s predicted from the FFT method for both models (k-ε and k-ω) is typically overestimated.



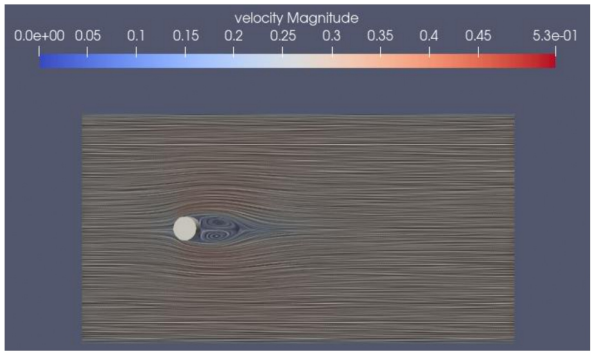


Fig 4.5 Velocity magnitude streamlines downstream of the circular pier at difference of 0.5 seconds using *k-ω* SST

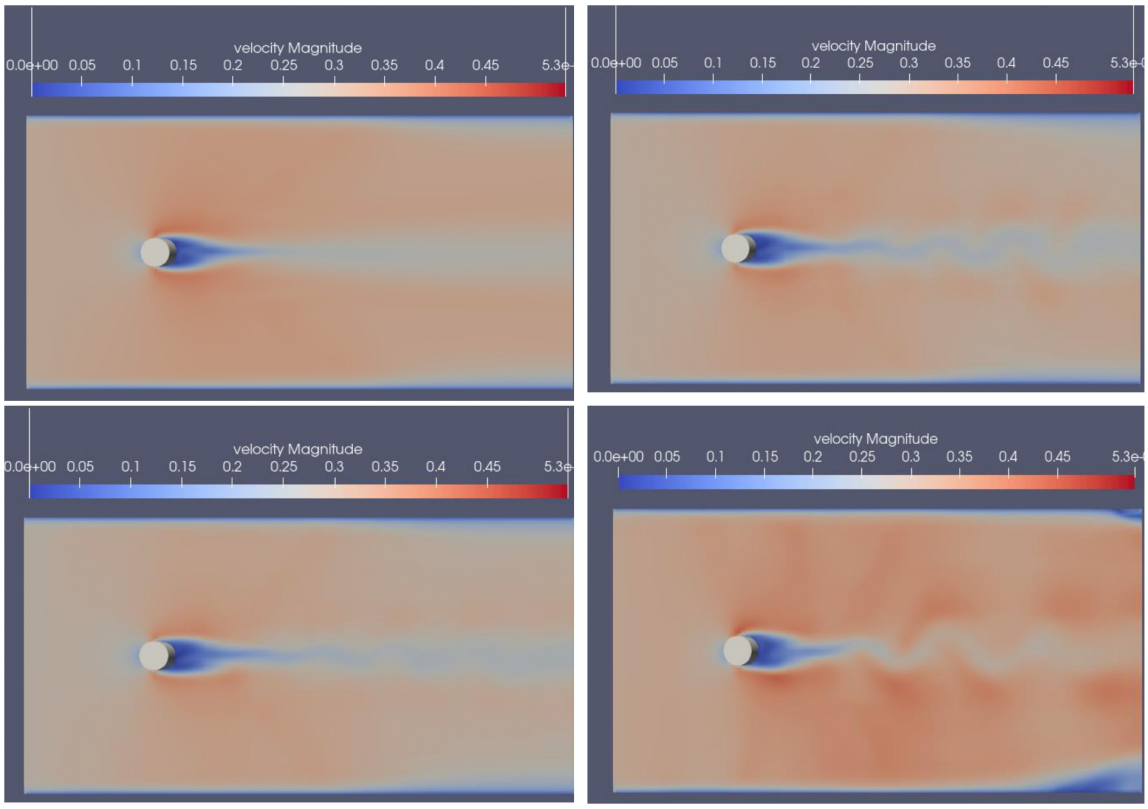


Fig. 4.6 velocity magnitude behind the circular pier at a difference of 0.5 seconds

4.3 Mean pressure distributions

The pressure coefficients for all the models upstream of the cylinder along the symmetry line are shown in Fig. 4.8. The data were averaged after 30,000 time-steps, or three flows through times, to ensure that the averaged figures are smooth. To obtain flow data, the simulation was then run 30,000 more times.

While there is a noticeable difference between the projected and experimental results of the k-ω SST and the k-ε standard model, all models are generally in good agreement. It is evident from Fig. 4.7 that this is because of the influence of the horseshoe vortices that URANS predicted would occur in this area.

The pressure coefficient's behavior profile is in good agreement with Dargahi's experimental data, as can be seen in the figure below, where the experimental results start to diverge at X/D = -0.86. The URANS model suggests a somewhat early separation of the flow in comparison to the experiment, which results in the vortex being sensed more upstream of the cylinder than measured. Similar differences were found in studies with URANS models for this flow with a k-ε turbulence model conducted by Tao (2013) and Roulund et al. (2005).

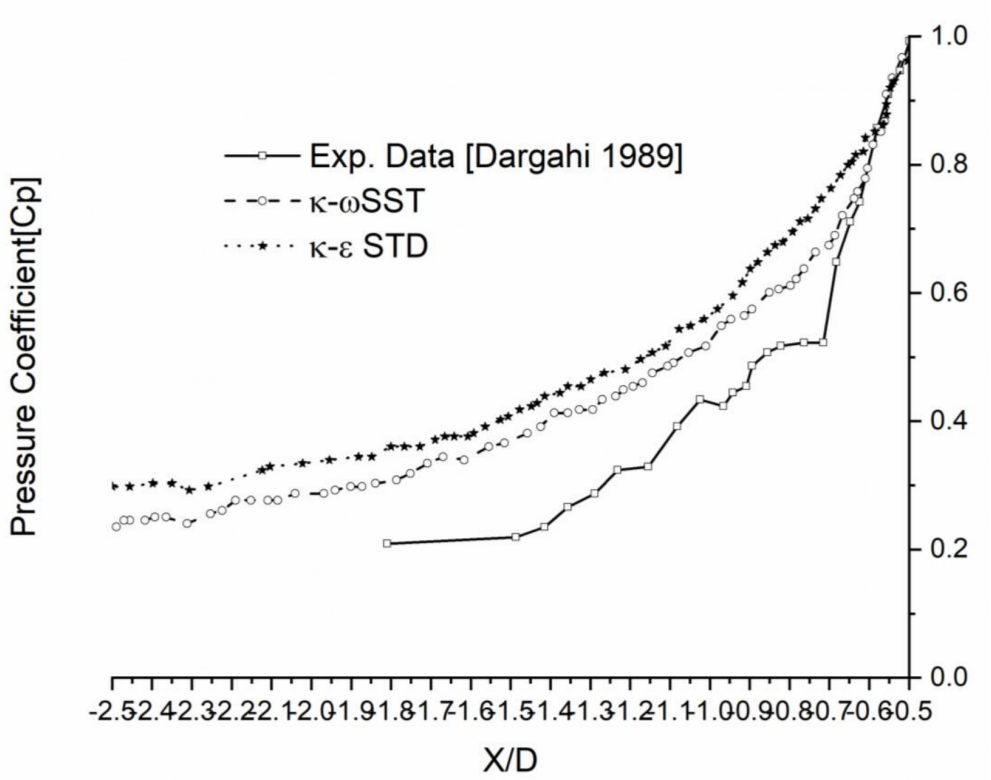


Fig 4.7 Pressure coefficient along the line of symmetry upstream of circular pier

The pressure distribution along the vertical face of the cylinder is considered in Fig. 4.8. While the lowest accuracy in capturing the minimum pressure with *k-ε* was found at roughly y/H = 0.05 with C_p = 0.47, the vertical profile of the pressure distribution for the k- ω with the finest grid size is near to the experimental measurement, with the minimum pressure at about y/H = 0.075, with C_p =0.55 as shown in Fig. 4.8.

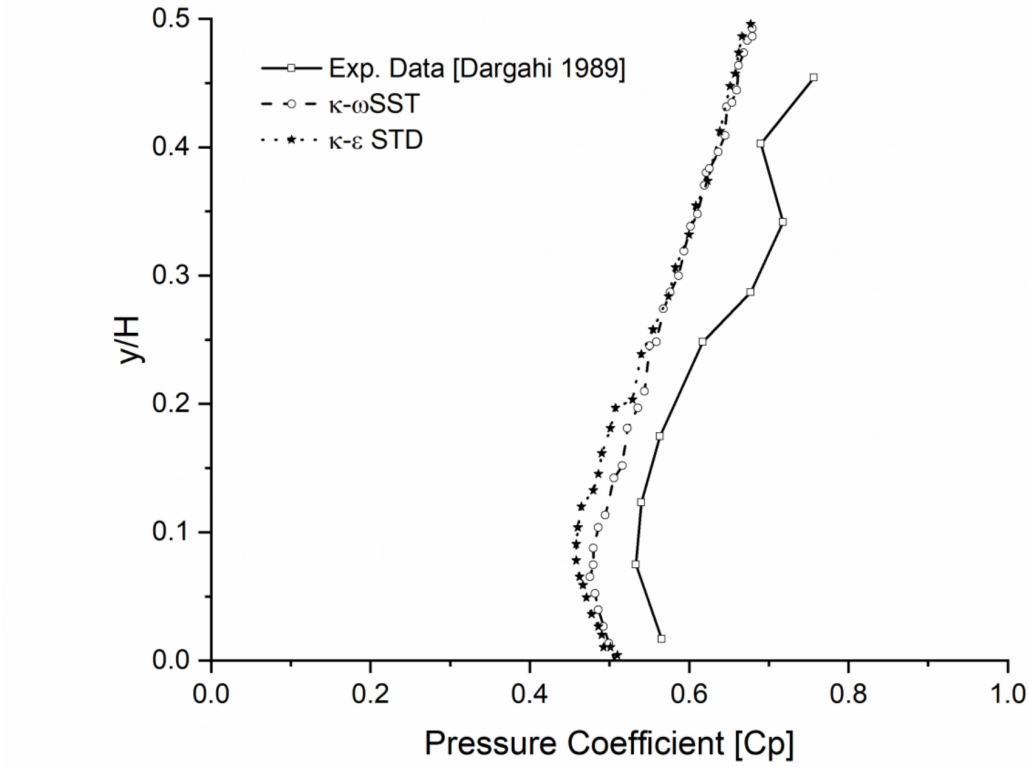


Fig 4.8 Pressure coefficient along the stagnation line at the upstream of a cylinder.

As the flow gets closer to the cylinder, the water level upstream of it starts to rise and peaks at the front face of the pier. This is due to the incoming flow slowing down, which results in the formation of an unfavorable pressure gradient and flow separation in both the horizontal and vertical planes.

Strong vortices in the wake region downstream of the cylinder cause the pressure to drop, which causes the water level to drop. The pier's influence on the water level in the area further from the cylinder gradually vanished.

Upstream of the cylinder, the pressure coefficient is positive, signifying a rise in both water level and pressure. As can be seen in Fig. 4.9, the distribution of the pressure coefficient at the free surface of the channel with the circular cylinder bridge pier, a negative pressure coefficient in the wake zone, downstream of the cylinder, indicates a drop in both water level and pressure. Equation 1.19 can be used to get the pressure coefficient C_p.

Figure 4.9 compares the CFD models used in this study with the experimental pressure coefficient at the free surface determined by Dargahi (1987) for a flow around a circular cylinder. It is evident that the k-ω, provides good accuracy when compared to other URANS models and experimental data.

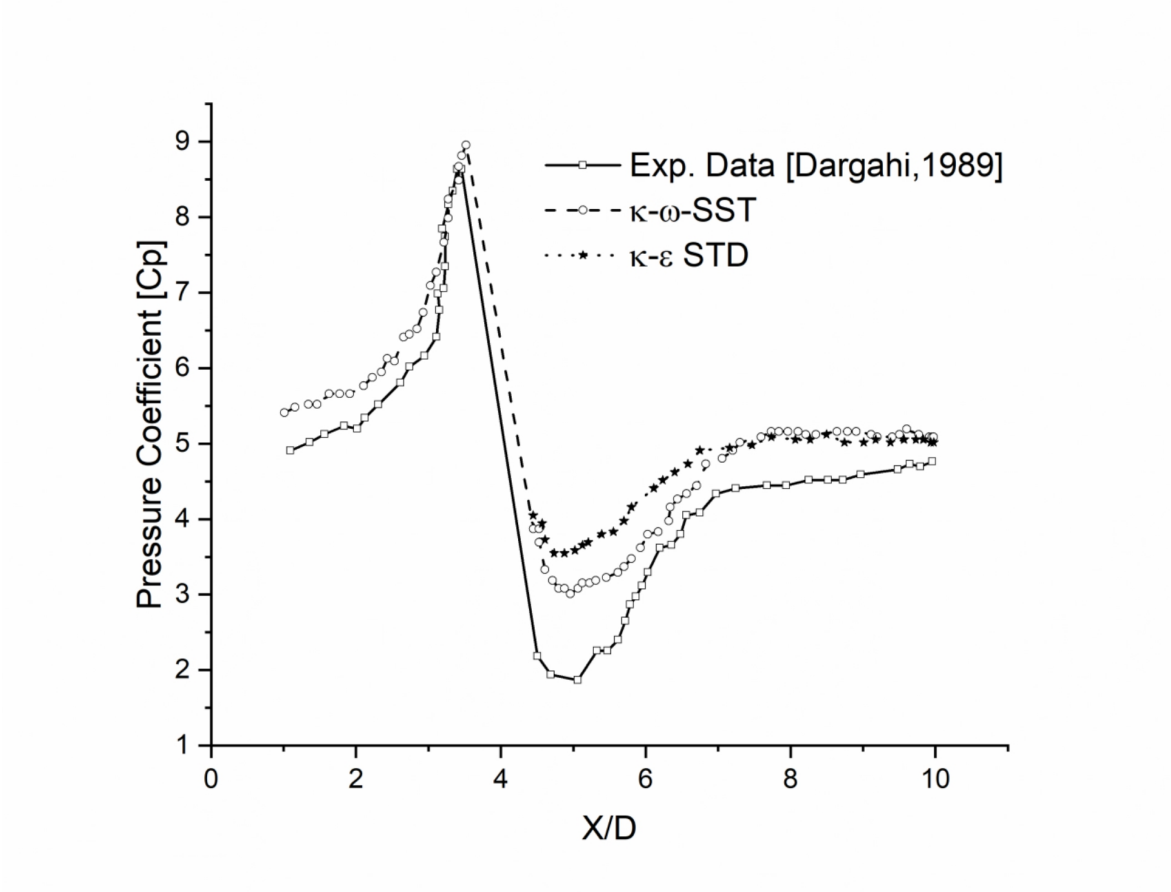


Fig 4.9 Pressure coefficient at the free surface and along the line of symmetry.

4.4 Bed shear stress

A comparison is made of the bed shear stress for each of the models in Fig 4.10. The results are normalised with the mean shear stress at a point located at X/D=-2.5 from the cylinder. The shear stresses are reduced as the cylinder is approached. All of the models generally exhibit good agreement with the experimental data. The k-SST model appears to yield a reasonable agreement with respect to the experimental value which is equal to 1.5, as shown in the figure when studying the amplification factor of the bed shear stress in the horseshoe vortex region with respect to the undistributed shear stress.

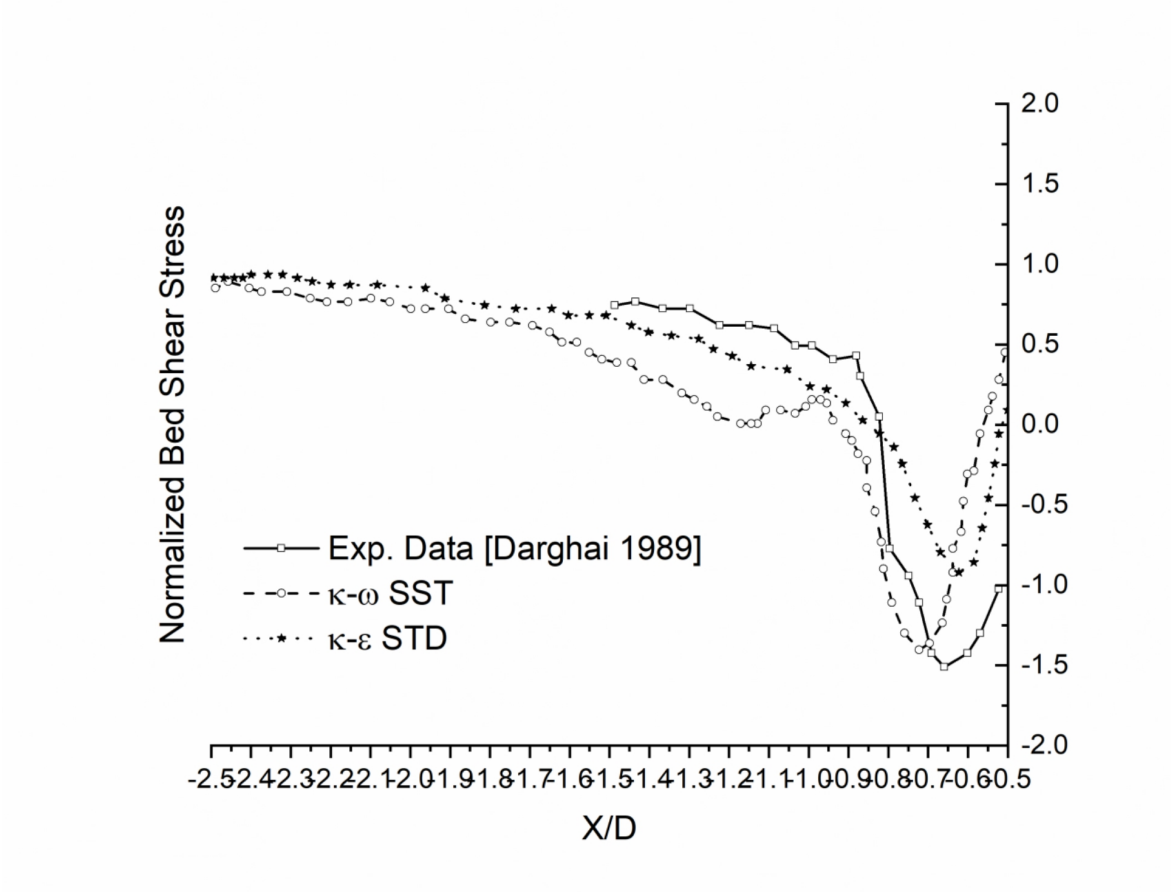


Fig 4.10 Mean bed shear stresses along the line of symmetry upstream of a cylinder.

4.5 Three-dimensional dynamics of the horseshoe vortex and scour mechanisms

The instantaneous vortices shown in Fig 4.11 reveal the 3D features of the horseshoe vortex with a disorganized thinner vortex closer to the cylinder and a well-organized thicker upstream vortex that has grown from the separation region. These two vortical structures correspond to the vortices V2 and V4 respectively.

In addition to these two primary vortices, V3 and V5 are secondary structures that form as a result of the interaction between the vortex and the wall, and V1 is a corner vortex at the base of the pier in the figure shown in Fig 4.3(c) for the symmetry plane.

Studying the transient behavior over a 30-second time period reveals that the vortices V2 and V1 are more stable than the vortices (V3, V4, and V5) found upstream of the primary vortex V2 and are located around the cylinder.

The wake zone downstream of the cylinder is also home to vortices in addition to the horseshoe vortex system upstream of it. Visualization of the instantaneous 3D coherent structures around the cylinder using K-SST is shown in Fig. 4.11.

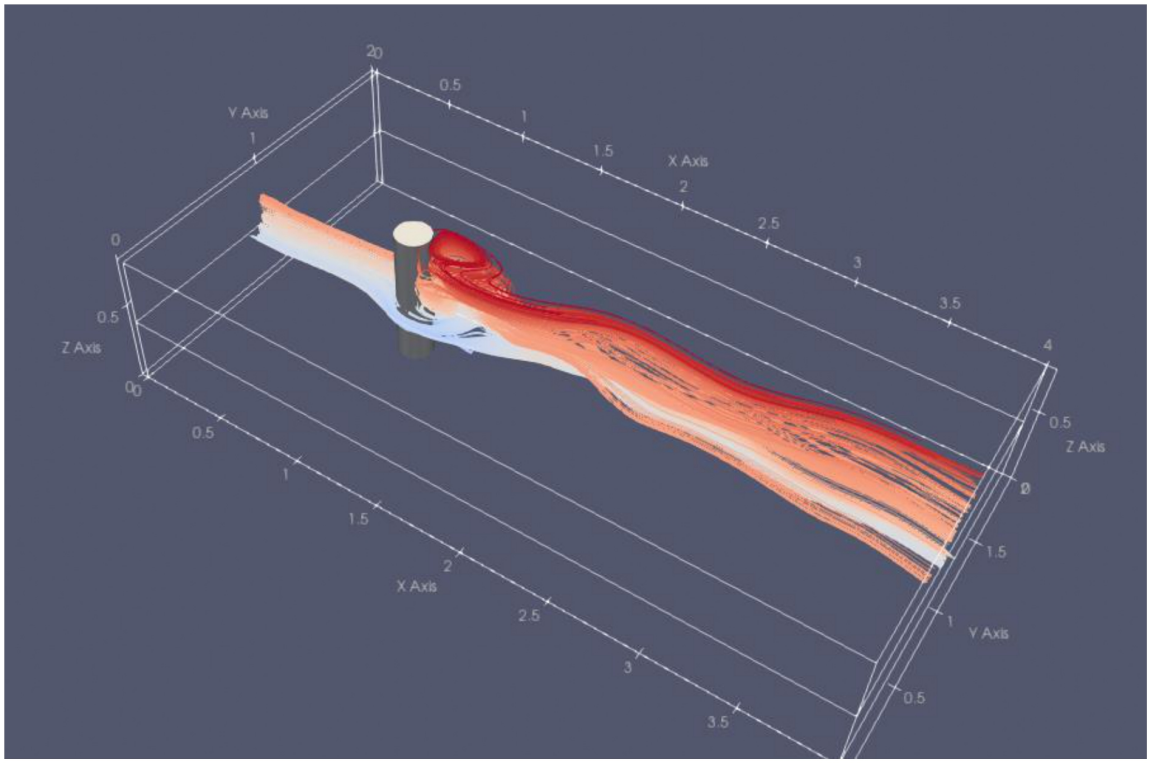


Fig 4.11 Visualization of the instantaneous 3D coherent structures around the cylinder using URANS models.

The temporal scour depth for the uniform graded sediment under clear water conditions shows a linear relationship with the rate of flow. The results of the temporal evolution of scour are shown in Fig 4.12. It shows the predicted maximum scour depth for the first 100 seconds from scour initiation using URANS. The maximum scour depth is recorded at the nose of the pier. However, the scour developed downstream of the pier is smaller than the scour hole developed at the upstream of the pier. The percentage of the difference between these two maximum scour depths at 100 seconds is about 10%, which is still considered acceptable compared to the time consumed in the case of k-SST compared to experimental data. With the rate of flow, the Froude number also increases whereas with the increase in the flow depth Froude number decreases and hence the scour depth increases. This trend has been observed in the case of the single pier, as shown in Fig. 4.12.

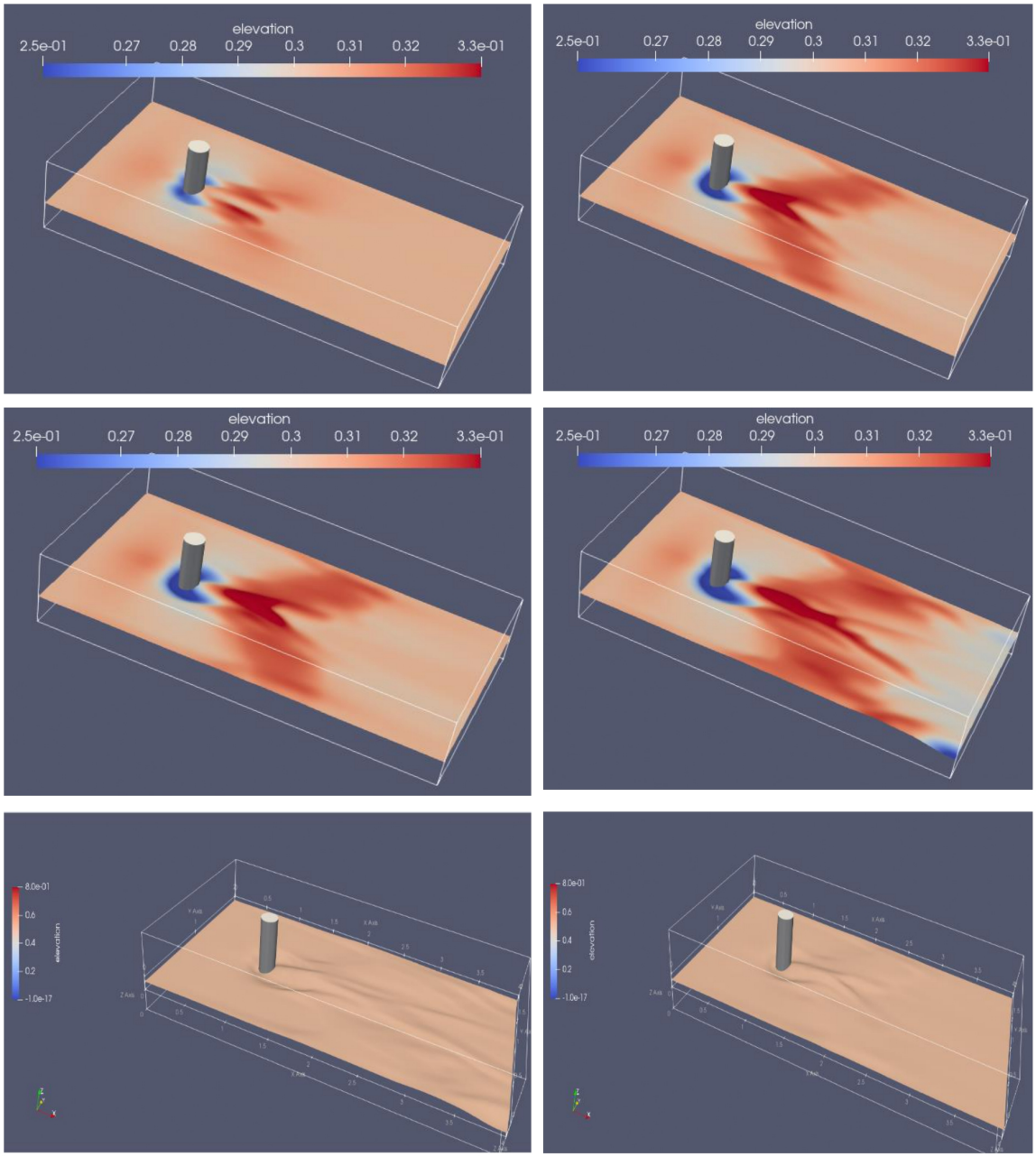


Fig 4.12 The maximum scour for the first 100 seconds of scour initiation using *k-ε* standard and *k-ω* SST

Chapter 5
Summary and findings

In this chapter, an eddy-resolving numerical model based upon the RANS approach has been implemented for predicting the 3D flow around a circular bridge pier, mounted on a flatbed, with $R_p=3.9\times10^4$. The experimental configuration by Dargahi (1989), was used for validation of the numerical results. Other validation data from the literature were used as well such as Dargahi (1987). The experimental results were compared with URANS models (i.e., k-ε standard and k-ω SST), and with the experimental data. It verifies the reliability and feasibility of the RANS to simulate the turbulent flow around obstacles mounted in a flatbed, given as:

The RANS model can capture all the horseshoe vortices upstream of the cylinder observed in Dargahi (1989). In contrast to the URANS models which show a single vortex at a distance of 0.85D from the front face of the cylinder. These horseshoe vortices consisting of two primary vortices identified as V2 and V4 located at a distance of 0.8D and 0.95D from the pier centre respectively, with their respective secondary structures that emerge due to the vortex-wall interaction, called V3 and V5 which located at 0.86D and 1.06D from the pier centre respectively, and a corner vortex at the base of the pier identified as V1. By studying the transient behavior of the horseshoe vortex system, it can be observed that V2 and V1 are the most stable vortices around the cylinder compared with the other vortices (V3, V4, and V5) which are found upstream of the main vortex V2.

In the case of comparing the time-averaged flow around the circular cylinder such as the velocity distribution profile downstream of the cylinder, the bed pressure coefficient, and the bed shear stress, all the models are in reasonable agreement with the experiments. However, it can be clearly observed that the RANS predictions are in very close agreement with the experiments.

Furthermore, the URANS predicts the vortex shedding in the wake of the cylinder, with a main frequency (and a corresponding Strouhal number 0.19) that is very close to the value reported by (Dargahi, 1989), which is equal to (0.1846). The mean drag coefficient for the entire pier is 1.19, and 1.24 for 12×10^6, and 24×10^6 grid sizes respectively. Although these values are somewhat higher than the value (1.15) derived from Dargahi (1989), it still predicts a very good estimation using URANS models such as k-ε standard (C_d=0.8) and k-ω SST (C_d =0.91) models.

Research into the energy spectrum density has been conducted for several locations near the cylinder and at various separations from the riverbed. It shows how accurate the simulation is in comparison to the experimental data.

This thesis proposes a simulation coupling methodology with a dynamic mesh technique. Using this technique, complex three-dimensional turbulent flow surrounding the bridge pier during bed sediment entrainments may be quantitatively studied. It gives additional information on the behavior of cohesive structures surrounding a bridge pier during the course of the scour process. When compared to previous numerical studies from the literature, this methodology is generally thought to be more effective for numerical

computations to anticipate the turbulent coherent structures surrounding the bridge pier during scour evolution.

In this case, the results of the simulation show the 3D development of the bed topography because of the flow past around the circular cylinder. The simulation induces most of the features reported by Dargahi (1990) during the initial stage of the scour around the cylinder such as:

The highest scour depth after 1000 seconds from the onset of scour, the maximum scour depth achieved in this study (2.4 cm) is marginally lower than the experimental value (3 cm). When compared to the maximum scour depth for the same flow and pier parameters, it still forecasts a very accurate estimate. Upstream of the cylinder, at around ±45° from the symmetry plane, is where the most scour happens.

After X=D upstream of the cylinder, where X is the distance between the scour hole's edge and the cylinder's front edge, no further scour happens. This is a result of the downflow's effect on the riverbed being disregarded beyond this point (X>D).

Additionally, throughout the evolution of scour, the flow field behavior surrounding the bridge pier is examined. The bed shear stress distribution around the cylinder alters as the scour process progresses, becoming less pronounced upstream and causing a notable shift on both sides of the cylinder. During scouring, the horseshoe vortex system characteristics have no considerable change. i.e.,

- The main vortex V2 which is trapped inside the scour region and the small vortex observed close to cylinder V1 are the most stable vortices around the bridge pier. Upstream of vortex V2 more vortices can be identified. These vortices behave in an irregular way.
- The main vortex V2 rotates such that the flow near the bed is towards the upstream whereas the flow near to the bed below V1 is towards the downstream. The counter-rotating of these two vortices (V1, and V2) has a significant effect on the scour developments upstream of the cylinder.
- The main horseshoe vortex V2 has the bimodal oscillation phenomenon which is captured using RANS. This phenomenon of moving the main horseshoe vortex forward and backward from the base of the bridge pier increases the ability of these vortices to entrain sediment.

The RANS technique is able to capture the pertinent physics of the flow dynamics during scour evolution, as demonstrated by all of the projected outcomes reported in this chapter. As so, it provides a clear understanding of the intricate relationship between the sediment movement and the coherent turbulence patterns of the flow surrounding the cylinder.

Chapter 6
Conclusions and Further Work

6.1 Conclusions

The flow field around a circular pier has been investigated computationally in a fully developed turbulent open channel flow. A simulation with the experimental configuration of Dargahi (1989) for turbulent channel flow past a circular cylinder mounted in a flatbed has been undertaken using the RANS approach. The predicted results were compared with those obtained from URANS models (i.e., *k-ε* standard and *k-ω* SST) with the experimental data. It verifies the reliability and feasibility of the URANS to simulate the turbulent flow around obstacles mounted on a flatbed river channel.

The following remarks were concluded:

- The URANS model can capture the full set of horseshoe vortices upstream of the circular pier model that was observed in Dargahi's (1989) experimental study.
- In the case of comparing the time-averaged predicted results around the circular pier model (the velocity distribution profile downstream of the circular pier model, the bed pressure coefficient and the bed shear stress), the results from URANS models are in reasonable agreement with the experiments.
- However, the k-ω SST predictions give closer agreement to the measured experimental values (the Strouhal number and the drag coefficient values) for the flow passing around the circular pier model.

The URANS technique has been undertaken to study the coherent structures around a circular bridge pier in the initial stage of scour evolution. The approach produces good predictions for qualitative and quantitative characteristics observed by Dargahi (1990); including:

- The maximum scour depth and its location from the symmetry plane.
- The scour pattern around the circular circular pier model.

6.2 Further Work

Certain parts of the research would benefit by applying additional alternative techniques. For example, simulations modelling of the scour around bridge piers by URANS with advanced sediment transport models (two-phase flow models which treat the sediment as a separate phase), would be something interesting to look at. Such models that simultaneously couple the fluid and particle phases are the future trend in the scour process simulation and its applications. However, due to the high demand for computational resources, RANS application is limited to the early stages of scouring around piers in flow with a medium Re (e.g. 3.9×10^4). In future, it's expected to see more research on scour at various stages of and in flow with higher R_e which are closer to real-life river conditions.

Further studies should be carried out on the effect of geometry on bridge piers. For example, flow and scour patterns around a group of piers with different configurations, such

as the distance between the piers. Due to very limited experimental studies at a laboratory scale, advanced numerical simulations are expected to provide more details on the mechanism of scour around complex structures and thus help to improve the design of bridge foundations and scour counter measures.

6.3 References

Abed, L. and Gasser M. M., (1993). "Model study of local scour downstream bridge piers." Proceedings National Conf. on Hydraulic Engineering, San Francisco, pp.1738–1743.

Ahmed, F., & Rajaratnam, N. (1998) "Flow around bridge piers" *Journal of Hydraulic Engineering*, 124(3), pp.288-300.

Arneson, L. A., Zevenbergen, L.W., Lagasse, P. F., and Clopper, P. E. (2012). "Evaluating scour at bridges." Hydraulic Engineering Circular no 18. Washington D.C., US.

Ataie-Ashtiani, B., and Beheshti, A. A. (2006). "Experimental Investigation of Clear-Water Local Scour at Pile Groups." *Journal of Hydraulic Engineering*, 132(10), pp.1100–1104.

Benedict, S. T., Deshpande, N., and Aziz, N. M. (2007). "Evaluation of Abutment Scour Prediction Equations with Field Data." *Transportation Research Record: Journal of the Transportation Research Board*, 2025(1), pp.118–126.

Breusers, H. N. C., Nicollet, G., & Shen, H. W. (1977). "Local scour around cylindrical piers." *Journal of Hydraulic Research*, 15(3), pp.211-252.

Breusers, H.N.C. and Raudkivi, A.J. (1991). *Scouring*. IAHR hydraulic structures design manual, Rotterdam, The Netherlands, 2.

Chen, W., Ji, C., Alam, M. M., Yan, Y., (2022) "Three-dimensional flow past two stationary side-by-side circular cylinders" *Ocean Engineering*, 244, pp.379-390.

Chien, N. 1999. *Mechanics of sediment transport.* Institute of Water Resources and Hydro-Power Research Translated under the guidance of John S. McNown Late Engineering College Dean, University of Kansas.

Chiew, Y. M. (2004). "Local scour and riprap stability at bridge piers in a degrading channel." *Journal of Hydraulic Engineering*, 130(3), pp.218–226.

Dargahi, B. (1987). "Flow field and local scouring around a pier." Bulletin No. TRITA-VBI, 137.

Dargahi, B. (1989). "The turbulent flow field around a circular cylinder" *Experiments in Fluids,* 8, pp.1-12.

Dargahi, B. (1990). "Controlling mechanism of local scouring." *Journal of Hydraulic Engineering,* 116, pp.1197-1214.

Das, R., Das, S., Jaman, H. and Mazumdar, A. (2019). "Impact of Upstream Bridge Pier on the Scouring Around Adjacent Downstream Bridge Pier." *Arabian Journal for Science and Engineering,* 44(5), pp.4359–4372

Das, S. and Mazumdar, A. (2015). "Turbulence flow field around two eccentric circular piers in scour hole." *International Journal of River Basin Management*, 13(3), pp.343-361

Das, S., Das, R. andMazumdar, A. (2013). “Comparison of characteristics of horseshoe vortex at circular and square piers.” *Research Journal of Applied Sciences, Engineering and Technology*, 5(17), pp. 4373-4387.

Das, S., Das, R., & Mazumdar, A. (2015). “Velocity profile measurement technique for scour using ADV.” In *Proceedings of the 2015 International Conference on Testing and Measurement: Techniques and Applications, TMTA*, pp. 249-252.

Das, S., Ghosh, S. and Mazumdar, A. (2014*a*). “Kinematics of Horseshoe Vortex in a Scour Hole around Two Eccentric Triangular Piers.” *International Journal of Fluid Mechanics Research*, 41(4), pp. 296-317.

Deng, L., and Cai, C. S. (2010). “Bridge Scour: Prediction, Modeling, Monitoring, and Countermeasures—Review.” *Practice Periodical on Structural Design and Construction*, 15(2), pp.125–134.

Dey, S. (1999). Time-variation of scour in the vicinity of circular piers. *Proceedings of the Institution of Civil Engineers-Water Maritime and Energy*, 136(2), pp.67-75.

Dey, S., & Raikar, R. V. (2007) “Characteristics of horseshoe vortex in developing scour holes at piers” Journal of Hydraulic Engineering, 133(4), pp.399-413.

Escauriaza, C. 2008. Three-dimensional unsteady modeling of clear-water scour in the vicinity of hydraulic structures: Lagrangian and Eulerian perspectives, ProQuest.

Ettema, R., Kirkil, G. & Muste, M. (2006). “Similitude of Large-Scale Turbulence in Experiments on Local Scour at Cylinders”. *Journal of Hydraulic Engineering,* 132(1), pp.33-40.

Federal Highway Administration. (1993). “Evaluating scour at bridges.” *Hydraulic Engineering Circular No. 18, Rep. No. FHWA-IP-90-017*, U.S. Dept. of Transportation, Washington, DC.

Froehlich, D. C. (1989). “Local scour at bridge abutments.” *Proc., 1989 National Conf. on Hydraulic Engineering*, ASCE, New York, pp.13–18.

Germano, M., Piomelli, U., Moin, P. & Cabot, W. H. 1991. “A dynamic subgrid-scale eddy viscosity model.” *Physics of Fluids A: Fluid Dynamics,* 3(7), pp.1760-1765.

Gidaspow, D., Bezburuah, R., and Ding, J. (1992). “Hydrodynamics of circulating fluidized beds, kinetic theory approach.” *Proc., 7th Engineering Foundation Conf. on Fluidization*, American Institute of Chemical Engineers, New York, pp.75–82.

Graf, W. H., & Istiarto, I. (2002) “Flow pattern in the scour hole around a cylinder” *Journal of Hydraulic Research*, 40(1), pp.13-20.

Guo, J. (2012) “Pier scour in clear water for sediment mixtures” *Journal of Hydraulic Research*, 50(1), pp.18-27.

Hinze, J. (1975). Turbulence McGraw-Hill. *New York,* 218.

Huber, F. (1991) “Update: bridge scour, Civil Engineering Magazine” *ASCE*, 61 (9), pp.62-63.

Jain, S.C. and Fischer, E.E. (1979). Scour around bridge piers at high Froude numbers. *Report. No. FHWA- RD-79-104, Federal Highway Administration. Washington D.C*

Kardan, N., Hassanzadeh, Y. & Hakimzadeh, H. (2012). “Comparison of dynamic bed shear stress distribution around a bridge pier using various turbulence models.” *ICSE6. Paris.*

Karimi, M., Qaderi, K., Majid Rahimpour, M., and Ahmadi, MM. (2020) "Laboratory Investigation of Effect of Collar on Scour at Bridge Piers Group and Abutment in the Presence of Debris." *Irrigation and Drainage Structures Engineering Research*, 21(78), pp.99-116.

Kassem, A., Salaheldin, T., Imran, J., and Chaudhry, M. (2003). "Numerical Modeling of Scour in Cohesive Soils Around Artificial Rock Island of Cooper River Bridge." *Transportation Research Record: Journal of the Transportation Research Board*, 1851(1), pp.45–50.

Kirkil, G., Constantinescu, S. & Ettema, R. (2008). "Coherent structures in the flow field around a circular cylinder with scour hole." *Journal of Hydraulic Engineering,* 134, pp.572-587.

Kothyari U. C. and Ranga Raju K. G. (2001) Scour around spur dikes and bridge abutments, *Journal of Hydraulic Research*, 39(4), pp.367-374.

Kothyari, U.C., Raju, K.G.R. and Garde, R.J. (1992*a*). Live-bed scour around cylindrical bridge piers. *Journal of Hydraulic Research*, 30(5), pp.701-715.

Kothyari, U.C., Raju, K.G.R. and Garde, R.J. (1992*b*). Temporal variation of scour around circular bridge piers. *Journal of Hydraulic Engineering*, 118(8), pp.1091-1106.

Kothyari, U. C., Hager, W. H., & Oliveto, G. (2007) "Generalized approach for clear-water scour at bridge foundation elements" *Journal of Hydraulic Engineering*, 133(11), pp.1229-1240.

Kumar, A., Kothyari, U. C., and Raju, K. G. R. (2012). "Flow structure and scour around circular compound bridge piers—A review." *Journal of Hydro-environment Research*, 6(4), pp.251–265.

Lagasse, P. F., and Richardson, E. V. (2001). "ASCE compendium of stream stability and bridge scour papers." *Journal of Hydraulic Engineering*, 127(7), pp.531–533.

Lilly, D. K. (1992). "A proposed modification of the Germano subgrid-scale closure method." *Physics of Fluids A: Fluid Dynamics,* 4, pp.633-635.

Link, O., Gobert, C., Manhart, M. & Zanke, U. (2008). "Effect of the horseshoe vortex system on the geometry of a developing scour hole at a cylinder." 4th International Conference on Scour and Erosion, Tokyo, pp.162-168.

Melville, B. and Sutherland, A. (1988). "Design method of time Dependent Local Scour at Circular Bridge Pier." *Journal of Hydraulic Engineering,*114(10), pp.1210-1226.

Melville, B. W. & Chiew, Y.-M. 1999. Time scale for local scour at bridge piers. *Journal of Hydraulic Engineering*, 125, pp.59-65.

Melville, B. W. & Raudkivi, A. J. (1977). "Flow characteristics in local scour at bridge piers." *Journal of Hydraulic Research,* 15, pp.373-380.

Melville, B. W. (1975). "Local scour at bridge sites." Ph.D. thesis, School of Engineering, Univ. of Auckland, Auckland, New Zealand.

Melville, B. W. (1997). "Pier and abutment scour: integrated approach." *Journal of Hydraulic Engineering,* 123, pp.125-136.

Melville, B.W. and Coleman, S.E. (2000). Bridge scour. *Water Resources Publications*, Fort Collins, Colorado, USA.

Menter, F. 2012. Best practice: scale-resolving simulations in ANSYS CFD. ANSYS Germany GmbH, pp.1-70.

Saharabian, M., Saharabian, A., Karakouzian, M. and Karami, M. (2020). “Sacrificial Piles as Scour Countermeasures in River Bridges A Numerical Study using FLOW-3D.” *Civil Engineering Journal*, 6(6), pp. 1091-1103.

Nieto, F., Hargreaves, D., Owen, J. S. & Hernández, S. (2015). “On the applicability of 2D URANS and SST k-ω turbulence model to the fluid structure interaction of rectangular cylinders.” *Engineering Applications of Computational Fluid Mechanics,* 9, pp.157-173.

Prasanna S V S N D L, and Suresh Kumar, N. (2018) Simulation of Flow Behaviour around Bridge Piers Using ANSYS – CFD.

Ramamurthy, A. S., Han, S. S., and Biron, P. M. (2013). “Three- dimensional simulation parameters for 90° open channel bend flows.” *Journal of Computing in Civil Engineering,* 27(3), pp.282–291.

Raudkivi, A. J., & Ettema, R. (1977). “Effect of sediment gradation on clear water scour.” *Journal of the Hydraulics Division*, 103(10), pp.1209-1213.

Raudkivi, A.J. (1986). “Functional trends of scour at bridge piers.” *Journal of Hydraulic Engineering*, 112(1), pp.1-13.

Richardson, E. V. (1999). “History of bridge scour research and evaluations in the United States.” *Stream Stability and Scour at Highway Bridges, Compendium of Papers, Water Resources Engineering Conf. 1991– 1998*, ASCE, Reston, VA.

Rodi, W., Constantinescu, G., & Stoesser, T. (2013). “Large-eddy simulation in hydraulics.” *Crc Press*, pp. 231-239.

Roulund, A., Sumer, B. M., Fredsøe, J. & Michelsen, J. (2005) “Numerical and experimental investigation of flow and scour around a circular pile.” *Journal of Fluid Mechanics,* 534, pp. 351-401.

Simões, F. J. (2014). “Shear velocity criterion for incipient motion of sediment.” *Water Science and Engineering,* 7, pp. 183-193.

Smagorinsky, J. (1963). “General circulation experiments with the primitive equations: I. The basic experiment.” *Monthly Weather Review,* 91, pp. 99-164.

Smith, D. (1976) “Bridge failures.” *Proceedings of Institution of Civil Engineers*, 60, pp. 367-382.

Tao, J. & Yu, X. B. (2014). “Flow and Scour Patterns around Bridge Piers with Different Configurations: Insights from CFD Simulations.” Geo-Congress 2014: Geo-characterization and Modeling for Sustainability. GSP 234. ASCE, pp. 2655-2664.

Tao, J. (2013). Fusion of numerical modeling and innovative sensing to advance bridge scour research and practice. Case Western Reserve University, 28078543.

Terrance, C., Zhiyin, Y., Lu, Y., (2021) “Computational Study of Flow around 2D and 3D Tandem Bluff Bodies” *Journal of Applied Computational Mechanics*, 7, pp. 528-534.

Tseng, M. H., Yen, C. L. & Song, C. (2000). Computation of three-dimensional flow around square and circular piers. *International Journal for Numerical Methods in Fluids,* 34, pp. 207-227.

Umbrell, E. R., Young, G. K., Stein, S. M., and Jones, J. S. (1998). “Clear-Water Contraction Scour under Bridges in Pressure Flow.” *Journal of Hydraulic Engineering*, 124(2), pp. 236–240.

van Rijn, L. C. (1984). “Sediment transport, part I: bed load transport.” *Journal of Hydraulic Engineering,* 110, pp. 1431-1456.

van Rijn, L. C. (1986). “Applications of sediment pick-up function.” *Journal of Hydraulic Engineering,* 112, pp. 867-874.

Wei, Z. & Huhe, A. (2006). “Large-eddy simulation of three-dimensional turbulent flow around a circular pier.” *Journal of Hydrodynamics, Series B,* 18, pp. 765-772.

Wen Xiong, Pingbo Tang, Bo Kong, C. S. Cai (2016) “Reliable Bridge Scour Simulation using Eulerian Two-Phase Flow Theory.” *Journal of Computing in Civil Engineering*, 30(5), 04016009.

Wilcox, D. (2006). Turbulence Modeling for CFD, La Canada, CA, USA: DCW Industries. Inc.

Xiong, W., Cai, C. S., and Kong, X. (2012). “Instrumentation design for bridge scour monitoring using fiber bragg grating sensors.” *Applied Optics*, 51(5), pp. 547–557.

Xiong, W., Cai, C. S., Kong, B., and Kong, X. (2016a). “CFD Simulations and Analyses for Bridge-Scour Development Using a Dynamic-Mesh Updating Technique.” *Journal of Computing in Civil Engineering*, 30(1), 04014121.

Yanmaz, A. M. & Altinbilek, H. D. (1991). “Study of Time-Dependent Local Scour around Bridge Piers.” *Journal of Hydraulic Engineering*, 117(10), pp. 1247-1268.

Younis, B. & Abrishamchi, A. (2014). “Three-dimensional turbulent vortex shedding from a surface-mounted square cylinder: Predictions with large-eddy simulations and URANS.” *Journal of Fluids Engineering,* 136, 060907.

Zaid Hadi Obeid, Dr. Abdul-Hassan K. Al-Shukur (2016) “3D Numerical Simulation of Local Scouring and Velocity Distributions around Bridge Piers with Different Shapes.” *Asian Academic Research Journal of Multidisciplinary*, 3(2), pp. 1-11.

Zhang, H., Nakagawa, H., Kawaike, K., and Baba, Y. (2009). “Experiment and simulation of turbulent flow in local scour around a spur dyke.” *International Journal of Sediment Research*, 24(1), pp. 33–45.